ENZ medium triggered collapse of Fano resonances and emergence of generalized nonreciprocal Kerker effects by subwavelength hybrid meta-atoms

Yiyun Chen,[1] Yaping Zhang,[1] Qingtao Ba,[1,2] Lingzhong Zhao,[1] Jiafei He,[1] Lin Zhang,[1] Qilin Luo,[1,3] and Shiyang Liu[1,*]

[1]*Key Laboratory of Optical Information Detecting and Display Technology, Zhejiang Normal University, Jinhua 321004, China*

[2]*Department of Physics and Institute of Electromagnetics and Acoustics, Xiamen University, Xiamen 361005, China*

[3]*Xiangsihu College, Guangxi University for Nationalities, Nanning 530225, China*

(Received 27 July 2023; revised 14 November 2023; accepted 27 November 2023; published 8 December 2023)

By delicately designing the subwavelength "meta-atoms," the corresponding scattering properties can be flexibly engineered and one may provide more degrees of freedom for the implementation of custom-made light-matter interaction. In this paper, the magnetic medium loaded subwavelength hybrid meta-atoms (HMAs) are constructed, which exhibit nonreciprocal Fano resonance for the HMA immersed in air background due to the interference of Mie resonances associated with the angular momentum channels (AMCs) $m = \pm 1$ as well as the combining interaction for the Mie resonances with the AMCs $m = \pm 1$ and -2. The introduction of the epsilon-near-zero (ENZ) medium as the background medium results in the collapse of nonreciprocal Fano resonance due to the narrowed Mie resonances with much larger quality factors. As a consequence, the multipolar Mie resonances are superimposed solely with the uniform zeroth order mode, where two close intersections exist with one of them behaving as the nearly reciprocal Kerker effects showing the forward scattering and the other one behaving as the generalized nonreciprocal Kerker effects (GNKEs) showing the transverse unidirectional scattering. In addition, the operating frequency can be flexibly regulated by controlling the bias magnetic field, giving rise to the transformation between the reciprocal and nonreciprocal Kerker effects, as well as the frequency reversing of GNKEs with regard to the lower and higher order multipolar Mie resonances. In addition, the GNKE can even be modulated into the unidirectional scattering at nearly arbitrary direction with exceptional contrast by altering the permittivity of the ENZ background medium. By further considering magneto-optical materials the phenomenon can be expected at the optical regime and the research is also instructive for nonreciprocal photonics and potential applications.

DOI: 10.1103/PhysRevB.108.235413

I. INTRODUCTION

Light scattering by subwavelength particles is a rather classical topic and it remains the fundamentally important issue in electrodynamics due to the close association with a variety of potential applications such as optical imaging [1,2], cancer management [3,4], and atmospheric research [5,6], as well as biosensing and bioengineering [7–10]. The concept of metamaterials and metasurfaces has opened a new landscape in photonics by delicately engineering the associated building blocks [11,12], which can also revolutionarily upgrade the scattering performance of a single particle by modeling subwavelength "meta-atoms" with exquisite structures. Different from a conventional homogeneous particle, the electric and magnetic multipolar resonances in meta-atoms can be arbitrarily tailored in principle. As a consequence, the constructive and destructive interference of the multipolar resonances can bring about the extreme scattering effect such as superscattering [13,14] and invisibility [15,16]. In addition, the interference of broadband bright mode and narrow band dark mode can also lead to the Fano resonances, which were widely observed in nanostructures [17,18]. These subwavelength photonic systems can be regarded, to some extent, as typical meta-atoms and a great deal of promising functionalities were implemented, including enhanced nonlinear effects [19,20], Fano laser [21,22], and optical micromanipulation [23,24], among others.

Besides scattering amplitude, scattering directivity is another important feature in characterizing light scattering by subwavelength particles, in which the directivity can be tailored straightforwardly by breaking the spatial symmetry of the scattering object [25–28]. For spatially symmetric particles, the scattering directivity can also be tailored by appropriately exciting the multipolar resonances so that the constructive and destructive interferences occur at different directions, resulting in the enhancement and weakening of the light field at opposite directions, corresponding to directional scattering [27,29,30]. The seminal work by Kerker and co-workers investigated the scattering by a hypothetical magnetic sphere, where the forward scattering was realized and the backward scattering was almost completely suppressed, known as the first type Kerker effect [31–33]. Similarly, the unidirectional scattering can be observed with the forward scattering suppressed and the backward scattering dominated, corresponding to the second type Kerker effect [34–36]. In particular, the bidirectional transverse scattering comes into appearance by suppressing both forward and backward scat-

*syliu@zjnu.cn

tering, which is referred to as the third type Kerker effect [37–39]. Based on the Kerker effect, a wide range of interesting phenomena and functionalities have been demonstrated, including wide-angle transparency [38], enhanced spin-orbit optical mirage [40], generalized Brewster effect [41], enhanced emission rate [42], near-infrared photodetector [43], directional photoluminescence [44], and directional radiation pattern in atomic antennas [45], among others. Hitherto, Kerker effect has gained tremendous impetus and been implemented ubiquitously in a variety of photonic systems far beyond the original proposal for magnetic sphere, including high-index dielectric symmetric particles [29,33,35,39,46,47], irregular shaped particles [27,48–50], and particle oligomers [51–54], as well as periodic or aperiodic metastructures [38,41–44,55–57].

As is well known, under the exertion of a bias magnetic field (BMF) magnetic particles exhibit nonreciprocal features due to the breaking of time-reversal symmetry (TRS) [58]. Therefore, a variety of nonreciprocal phenomena and associated functionalities were implemented such as nonreciprocal scattering at the interface of magnetic metamaterials [59,60], nonreciprocal perfect absorbing effect [61,62], nonreciprocal edge states [63–65], nonreciprocal waveguiding [66–68], and nonreciprocal coupling effect supported by magnetic metasurfaces [69–71], as well as nonreciprocal add-drop filter [72,73]. Although the Kerker effect by magnetic particles was investigated theoretically and experimentally [31,34], the nonreciprocity-related properties were not evidently demonstrated. In this work, the magnetic medium loaded (MML) subwavelength hybrid meta-atoms (HMAs) are constructed, which exhibit nonreciprocal Fano resonances for the meta-atoms immersed in air background due to the degeneracy lift of multipolar resonances associated with the angular momentum channels (AMCs) of opposite signs. Compared to the traditional Fano resonance, the nonreciprocal Fano resonance can be controlled by a BMF and the nonreciprocal performance can also be expected. Zero-index materials were shown to remarkably modulate light-matter interactions, which include, among other things, the enhancement of light scattering [74,75] or, in turn, the diminishment of light scattering [76–78]. In addition, the epsilon-near-zero (ENZ) medium was shown to be capable of manipulating the multipolar resonances so that the enhancement of the thermo-optic effect [79], optical nonlinearity [80], and light confinement [81] were demonstrated. By altering the background medium from air to ENZ medium, the linewidths of multipolar Mie resonances turn out to be infinitely small, corresponding to the much larger quality factors, giving rise to the collapse of nonreciprocal Fano resonances. Meanwhile, the superimposition of multipolar modes with the nearly uniform zeroth order mode leads to the directional scattering at nearly arbitrary direction but at opposite direction the scattering is completely suppressed, indicating the emergence of the generalized Kerker effect. Interestingly, there exist two close intersections between the narrowed multipolar Mie resonance and the uniform zeroth order mode, where the scattering field at one intersection behaves seemingly as normal reciprocal Kerker effect as an ordinary dielectric particle, while the scattering field at the other intersection exhibits evident nonreciprocity with the associated directivity switchable by the orientation of BMF, thus termed generalized nonreciprocal Kerker effect (GNKE). In addition, the operating frequency can be flexibly regulated by tuning the magnitude of BMF and the nonreciprocal features can also be further modulated by the ENZ medium. By considering magneto-optical materials the phenomenon can be expected at the optical regime and the research is also instructive for the nonreciprocal photonics and potential applications. Interestingly, the oligomers made up of multiple HMAs or the metastructures constructed by periodically arranged HMAs can be investigated in the future to provide more fascinating phenomena.

II. NONRECIPROCAL FANO RESONANCES OF THE SUBWAVELENGTH HMAs

As a beginning, we first consider the architecture of the meta-atoms to be investigated in the present work. To implement the nonreciprocal scattering of a subwavelength particle, we introduce the magnetic medium as one of the constituents of the multilayered cylindrical particle so that an MML subwavelength HMA is designed, which offers an additional degree of freedom to optimize the nonreciprocal electromagnetic properties. Ferrite materials are typical magnetic media with the magnetic permeability tunable by a BMF [82,83] and under saturation magnetization the corresponding permeability is a second-rank tensor [84]

$$\hat{\mu} = \mu_s \begin{pmatrix} \mu_r & -i\mu_\kappa & 0 \\ i\mu_\kappa & \mu_r & 0 \\ 0 & 0 & 1 \end{pmatrix}, \tag{1}$$

with

$$\mu_r = 1 + \frac{\omega_m(\omega_0 - i\alpha\omega)}{(\omega_0 - i\alpha\omega)^2 - \omega^2}, \quad \mu_\kappa = -\frac{\omega_m\omega}{(\omega_0 - i\alpha\omega)^2 - \omega^2}, \tag{2}$$

where ω is the circular frequency of an incident electromagnetic wave, α is the damping factor closely related to material loss, $\omega_0 = 2\pi f_0 = 2\pi\gamma H_0$ is the spin-wave resonance frequency with $\gamma = 2.8$ MHz/Oe the gyromagnetic ratio and H_0 the BMF, and $\omega_m = 2\pi f_m = 2\pi\gamma M_s$ is the characteristic frequency with M_s the saturation magnetization. As a kind of widely used ferrite material, single-crystal yttrium iron garnet (YIG) is a good candidate to furnish the gyromagnetic property, which has the saturation magnetization $M_s = 1750$ G and the relative permittivity $\varepsilon_2 = 15$. As schematically shown in Fig. 1, the MML subwavelength HMA is a three-layered composite rod with the in-between layer the magnetic medium. The scattering properties of the HMA can be solved exactly within the framework of Mie theory as elaborately detailed in the Appendix. The Mie coefficients are given in Eqs. (A20) and (A23), based on which the dimensionless normalized scattering cross section (NSCS) Q_{sca} and the angular scattering amplitude (ASA) $\Gamma(\theta)$ measuring the scattering performance can be acquired.

To investigate the nonreciprocal properties of subwavelength HMAs, two kinds of HMAs are designed with the first kind of meta-atom possessing the parameters $\varepsilon_1 = \varepsilon_3 = 8$, $\mu_1 = \mu_3 = 1$, $r_1 = 4.7$ mm, $r_2 = 7.5$ mm, and $r_s = 9$ mm. The particle is immersed in the air and the scattering feature

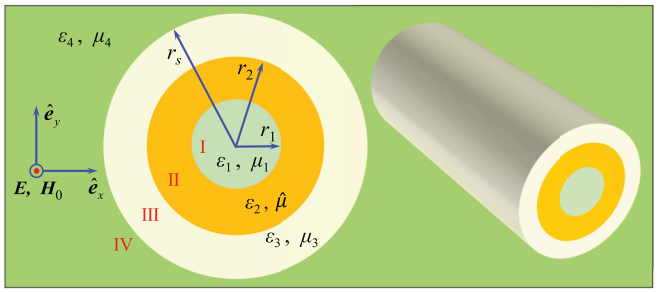

FIG. 1. Schematic diagram and the cross section of an MML subwavelength HMA illuminated by the incident electromagnetic wave of transverse magnetic (TM) polarization. The electric field is polarized along the rod axis, i.e., the z axis, and the layer radius r_i and corresponding constitutive parameters ε_i, μ_i are denoted as well. The radius of the third layer corresponds to the size of the outmost layer, identified by r_s to represent the radius of HMA and the permeability of the second layer corresponds to that for the magnetic layer, identified by $\hat{\mu}$ to indicate its gyromagnetic properties. The background is an isotropic dielectric medium with the relative permittivity ε_4 and the relative permeability μ_4, which is chosen as either the air or the ENZ medium to realize different scattering behaviors. H_0 is the BMF, exerted along the z axis.

is examined by calculating the NSCS Q_{sca} under a BMF $H_0 = 700$ Oe. The result is shown in Fig. 2(a), where the most prominent characteristic is the emergence of the asymmetric Fano dip in the vicinity of 4.9 GHz. From the partial wave NSCS associated with the AMCs $m = \pm 1$, a similar Fano dip can be found as identified by the blue solid line, suggesting that the multipolar modes corresponding to the AMCs $m = \pm 1$ play the crucial role. The slow variation of partial wave NSCS for $m = 0$ and ± 2 only increases the magnitude of total NSCS, serving as a background. Actually, in this case the higher order multipolar modes for $m = \pm 2$ are vanishingly small as indicated by the near-zero amplitude of the corresponding Mie coefficients in Fig. 2(b). To discover the origin of Fano resonance, the amplitudes $|S_m|$ and the phases Φ_m of Mie coefficients are plotted as the functions of the operating frequency f as shown in Figs. 2(b) and 2(c), where the Mie coefficients associated with $m = +1$ and $m = -1$ are evidently different, indicating the TRS breaking of the HMA, which does not appear for an isotropic dielectric particle. The degeneracy lift of the HMA arises from the nonreciprocal nature of the magnetic medium under the exertion of a BMF. In addition, it can be found that both the amplitude $|S_{-1}|$ and the phase Φ_{-1} are nearly unchanged in the vicinity of the Fano dip, behaving as the broadband bright mode, while for the multipolar mode with $m = +1$ both the amplitude $|S_{+1}|$ and the phase Φ_{+1} exhibit sharp change around the Fano dip, behaving as the narrow band dark mode. As a result, the interference of these two modes leads to the formation of Fano resonance, termed nonreciprocal Fano resonance due to the TRS breaking nature of HMAs under a BMF.

For the first kind of HMA only the lower order modes contribute evidently to the nonreciprocal Fano resonance. To examine the influence of the higher order modes the second kind of HMA is taken into account, for which the inner radius of the in-between magnetic layer is changed to be

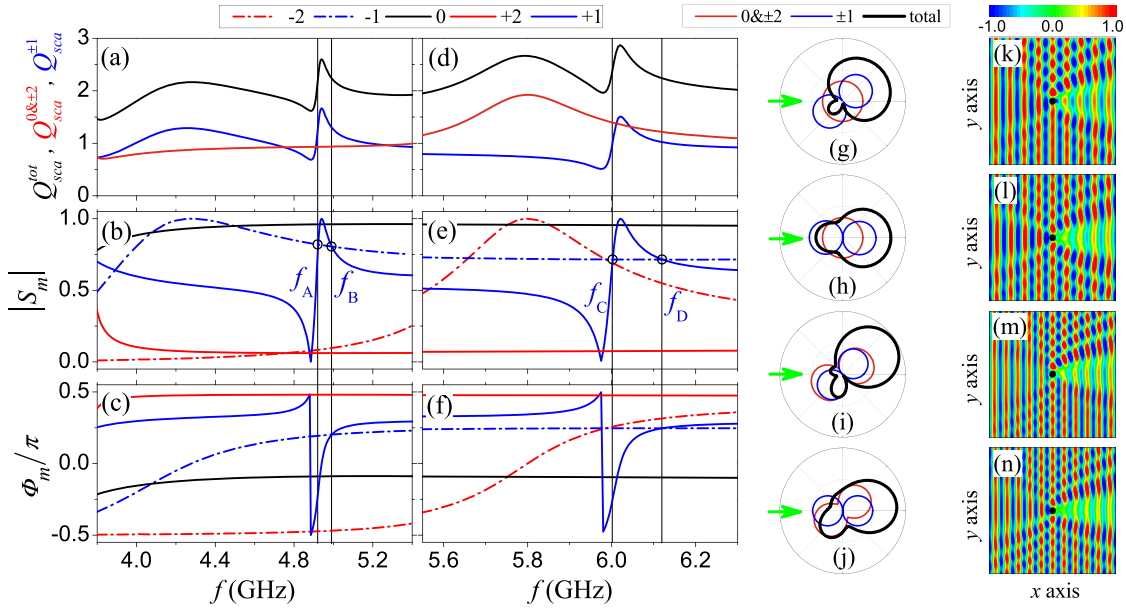

FIG. 2. Total NSCS $Q_{\text{sca}}^{\text{tot}}$, the partial NSCSs $Q_{\text{sca}}^{0\&\pm2}$ and $Q_{\text{sca}}^{\pm1}$ associated, respectively, with the AMCs $m = 0, \pm2$ and $m = \pm1$ (a), (d), as well as the amplitude $|S_m|$ (b), (e) and the phase Φ_m (c), (f) of Mie coefficients plotted as the functions of the operating frequency f for the first (a)–(c) and second (d)–(f) kind of HMA immersed in the air, respectively, under the exertion of a BMF $H_0 = 700$ Oe. The ASAs $\Gamma(\theta)$ together with the electromagnetic field patterns are plotted at four typical frequencies f_A (g), (k), f_B (h), (l), f_C (i), (m), and f_D (j), (n) for two kinds of HMAs. The hollow circles in panels (b) and (e) mark the chosen frequencies f_A, f_B, f_C, and f_D. The green arrows in panels (g)–(j) mark the direction of incident electromagnetic waves and the black solid circles in panels (k)–(n) mark the positions of the HMAs. The related parameters are $\varepsilon_1 = \varepsilon_3 = 8$, $\mu_1 = \mu_3 = 1$, $r_2 = 7.5$ mm, $r_s = 9$ mm, $\varepsilon_2 = 15$, and $M_s = 1750$ G. For the first kind of HMA the radius of the dielectric core is $r_1 = 4.7$ mm and the radius of the dielectric core is $r_1' = 2.88$ mm for the second kind of HMA.

$r_1' = 2.88$ mm, corresponding to the increase of the layer thickness. In this case, the NSCS also exhibits evident Fano dip in the vicinity of 5 GHz as indicated by the black solid line in Fig. 2(d). Compared to the partial wave NSCS, besides the main contribution from that corresponding to the AMCs $m = \pm 1$ the partial wave NSCS associated with the AMCs $m = 0$ and $+2$ also contributes somewhat to the nonreciprocal Fano interference. By examining the amplitude $|S_m|$ and the phase Φ_m of Mie coefficients in Figs. 2(e) and 2(f), it can be found that the multipolar mode with $m = -1$ still behaves as the broadband bright mode and that for $m = +1$ is the narrow band dark mode. However, different from the first kind of HMA the multipolar mode associated with the AMC $m = -2$ behaves as an intermediate mode as indicated by the red dashed line. As a consequence, the combinational interaction of the multipolar modes for $m = \pm 1$ and $m = -2$ gives rise to the occurrence of nonreciprocal Fano interference and thus the NSCS undergoes a certain increase compared to the first kind of HMA. Actually, the nonreciprocal Fano resonance can also be engineered by tuning the permittivities of the dielectric layers, thus offering more degrees of freedom.

To vividly visualize the physical consequences of nonreciprocal Fano resonance, the scattering feature is investigated by calculating the ASAs and the electric field patterns for the aforementioned two kinds of HMAs illuminated by the incident plane waves of TM polarization. Regarding the first kind of HMA two typical operating frequencies f_A and f_B are chosen at the intersections of $|S_m|$ for the AMCs $m = \pm 1$, as marked by the hollow circles in Fig. 2(b). The corresponding ASAs are plotted in Figs. 2(g) and 2(h), respectively, where the upper rightward scattering is demonstrated at frequency f_A, signifying the nonreciprocal characteristic. Differently, at frequency f_B the nearly symmetric forward scattering can be observed with $\Gamma(\theta) = \Gamma(-\theta)$, which is similar to the scattering behavior of an isotropic dielectric particle, signifying the reciprocal characteristic. Considering the fact that the zeroth order mode does not possess the nonreciprocal feature, thus the multipolar modes with the AMCs $m = \pm 1$ play the crucial role for the implementation of nonreciprocal performance, which can be corroborated by the asymmetric and symmetric figure-of-eight profiles of ASAs with respect to the incident direction as indicated by the blue solid lines in Figs. 2(g) and 2(h), respectively. Later on, it will be shown that the phase difference of the multipolar modes determines the directivity of scattering field for a pair of partial waves. Regarding the second kind of HMA, the chosen frequencies are still positioned at two intersections f_C and f_D of $|S_m|$ for the AMCs $m = \pm 1$ as marked by the hollow circles in Fig. 2(e). The corresponding ASAs are shown in Figs. 2(i) and 2(j), respectively, where the ASA from the partial waves with $m = \pm 1$ exhibits a similar behavior as that of the first kind of HMA. Differently, the ASAs from the partial waves with $m = 0$ and $m = \pm 2$ manifest themselves as asymmetric profiles with respect to the incident direction, indicating the nonreciprocal feature at both frequencies f_C and f_D due to the evident contribution from the multipolar mode with $m = -2$. As a consequence, the unidirectional scattering is enhanced at frequency f_C and at frequency f_D a weakened nonreciprocal feature still exists. The nonreciprocal scattering features can also be visualized by examining the corresponding electric field profiles as shown in Figs. 2(k)–2(n), where the evident asymmetric interference patterns in panels (k) and (m) are in good agreement with the corresponding ASAs. In addition, the scattering amplitudes are still very strong, as can be verified by the large shadows behind the HMAs, although the superscattering with the superimposed Mie resonances is not achieved.

It is noted that from the scattering features shown in Figs. 2(g)–2(n) there appears evident backward scattering, which, actually, can be diminished by simply examining the scattering behaviors at other specified operating frequencies for the first and second kinds of HMAs. In this occasion, the forward scattering is dominated, similar to the first type Kerker effect, but the scattering amplitude is relatively weak. In addition, by tuning the BMF H_0 the corresponding operating frequency can be continuously adjusted. However, the nonreciprocity is much weaker compared to the scattering behaviors in the vicinity of nonreciprocal Fano resonances. Interestingly, by further engineering the geometric parameters of HMAs the NSCS can be improved, corresponding to the superposition of a part of Mie resonances. Nonetheless, in such occasion the scattering profiles are nearly symmetric with respect to the incident direction and the nonreciprocal Fano resonances cannot be established. Another matter usually concerned is the bandwidth of operating frequency, which seems to be a single frequency since the operating frequency is chosen at the intersections of Mie resonances in the numerical simulations. Actually, in the vicinity of the chosen frequency the similar but relatively weaker effect can still be observed although the bandwidth is still narrow. Nonetheless, this feature is beneficial to the tunability of operating frequency by controlling the BMF. By increasing the refractive index of the background medium, the bandwidth of operating frequency can be augmented somewhat but it cannot bring about qualitative change. On the contrary, the decrease of background medium to zero refractive index can initiate substantially different physical consequences, which will be investigated intensively in the following sections.

III. GENERALIZED NONRECIPROCAL KERKER EFFECTS DUE TO ENZ MEDIA

Considering the fact that the near-zero index material can substantially change the scattering properties, we turn to investigate the situation for the subwavelength HMAs immersed in the ENZ materials for convenience. The scattering properties for the first kind of HMA are shown in Fig. 3, where we can find that the asymmetric Fano dip appearing in the NSCS Q_{sca} can no longer be discerned for the ENZ medium with the relative permittivity $\varepsilon_4 = 0.04$ as shown in panel (f) and completely vanishes for an even smaller permittivity $\varepsilon_4 = 0.0025$ as shown in panel (i). To interpret the collapse of nonreciprocal Fano resonance, the phase diagrams for the Mie coefficients with respect to the background refractive index n and the operating frequency f are plotted and the results are shown in Figs. 3(a)–3(c) regarding the lower order AMCs $m = 0$ and ± 1. It can be found that the amplitude of zeroth order $|S_0|$ uniformly decreases with decreasing the background refractive index n ($n^2 = \varepsilon_4$), while the amplitude undergoes nearly no change in the considered frequency range. Differently, the amplitudes $|S_{\pm 1}|$ of Mie coefficients exhibit distinct

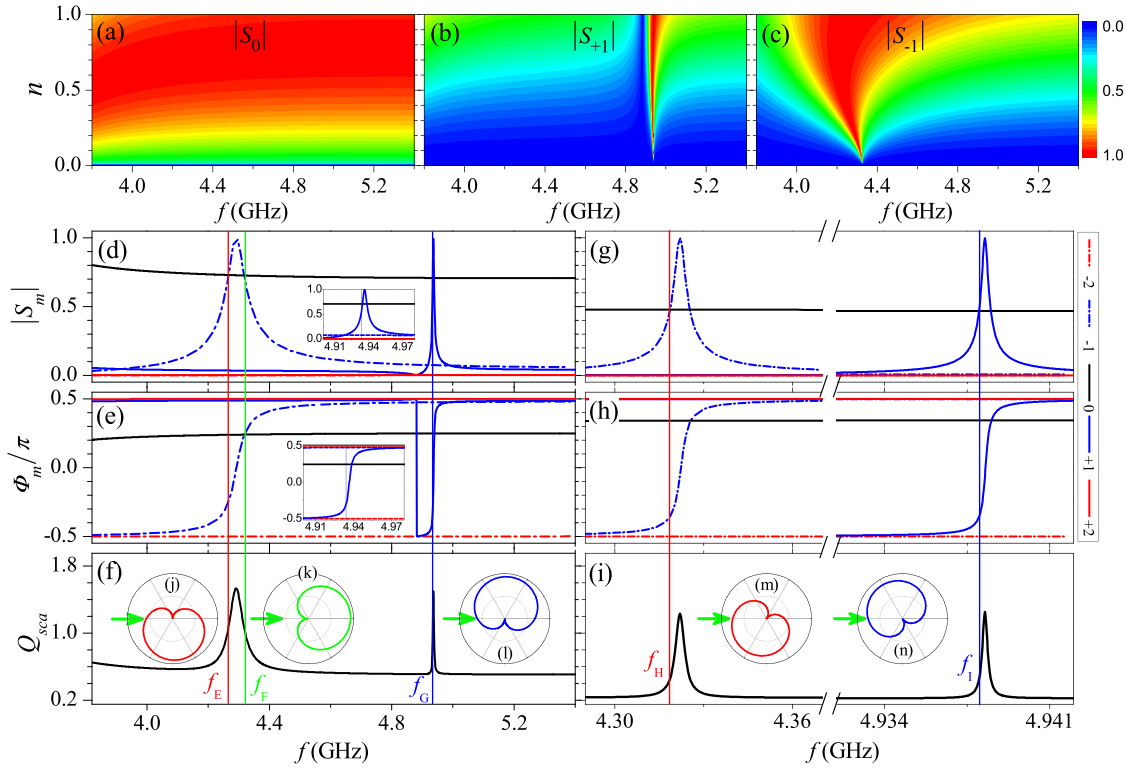

FIG. 3. Phase diagrams for the amplitudes (a) $|S_0|$, (b) $|S_{+1}|$, and (c) $|S_{-1}|$ of Mie coefficients with respect to the operating frequency f and the refractive index n of the background medium are plotted for the first kind of HMA under the BMF $H_0 = 700$ Oe. The amplitudes $|S_m|$ (d), (g) and the phases Φ_m (e), (h) of Mie coefficients are plotted as the functions of the operating frequency f for the ENZ background medium with the relative permittivity (d), (e) $\varepsilon_4 = 0.04$ (refractive index $n = \sqrt{\varepsilon_4} = 0.2$) and (g), (h) $\varepsilon_4 = 0.0025$ (refractive index $n = 0.05$), respectively. The insets in panels (d) and (e) are the amplified view of the curves in the vicinity of the narrow Mie resonance with $m = +1$. The NSCS Q_{sca} is plotted as the function of the operating frequency f for the ENZ background medium with the relative permittivity (f) $\varepsilon_4 = 0.04$ (refractive index $n = 0.2$) and (i) $\varepsilon_4 = 0.0025$ (refractive index $n = 0.05$), respectively, to illustrate the collapse of the nonreciprocal Fano resonance. Five typical operating frequencies f_{E}, f_{F}, f_{G}, f_{H}, and f_{I} are chosen and the corresponding ASAs are plotted in the insets (j), (k), (l), (m), and (n), respectively. The solid vertical lines mark the positions of operating frequencies and the green arrows denote the direction of the incident electromagnetic wave. All the other parameters are the same as those in Fig. 2.

change with the variation of permittivity ε_4 and operating frequency f as shown in Figs. 3(b) and 3(c), where the evident resonances come into appearance and the resonant linewidths in both cases become narrower and narrower with the decrease of background permittivity ε_4. In particular, when the background medium turns out to be an ENZ material the resonant linewidth is close to zero, suggesting an infinitely large quality factor for the ± 1st order Mie resonance.

Then, for two special ENZ background media with the relative permittivities $\varepsilon_4 = 0.04$ and 0.0025, the amplitudes $|S_m|$ and the phases Φ_m of Mie coefficients are plotted as the functions of operating frequency f. The results are shown in Figs. 3(d) and 3(e) and Figs. 3(g) and 3(h), respectively, where the Mie resonances with $m = -1$ and $m = +1$ are nearly separated for $\varepsilon_4 = 0.04$ and completely isolated for the ENZ material with even smaller permittivity $\varepsilon_4 = 0.0025$. As a result, the interaction between two Mie resonances with $m = \pm 1$ nearly vanishes, thus resulting in the collapse of nonreciprocal Fano resonances existing for the case of air background. This phenomenon is similar to that reported in the previous research, where the Fano resonance collapses into a bound state in the continuum for the photonic structures with the infinite quality factor [85].

It is of great importance to find out what the physical consequence is of the collapse for the nonreciprocal Fano resonance. For the ENZ material with $\varepsilon_4 = 0.04$, three typical operating frequencies f_{E}, f_{F}, and f_{G} are chosen as marked by the red, green, and blue solid lines, respectively, in panel (d), corresponding to the intersections between the zeroth order mode and the Mie resonances with $m = \pm 1$. The inset in panel (d) displays the amplified view of the narrower Mie resonance with $m = +1$ and the marked intersection corresponds to the chosen frequency f_{G}. The ASAs at three frequencies are plotted as shown, respectively, in the insets (j), (k), and (l), respectively, where the cardioid lines along different directions are demonstrated. At frequency f_{F}, the forward scattering is presented and the backward scattering tends to be zero, corresponding to the first type Kerker effect. Differently, at frequency f_{E} the transverse downward scattering is observed and at the opposite upward direction the scattering is vanished, which is not the aforementioned three types of Kerker effects and, specially, the remarkably nonreciprocal characteristic comes into emergence. As a result, this extraordinary scattering effect is termed GNKE; in particular, the directivity can be reversed by reversing the direction of BMF. At frequency f_{G}, the transverse upward scattering can be observed

as shown in inset (l), indicating that the GNKE is directed toward the opposite direction for the Mie resonances with opposite AMCs, signifying the nonreciprocal performance of the subwavelength HMA. Interestingly, for the background ENZ with the smaller permittivity $\varepsilon_4 = 0.0025$, the directions of unidirectional scattering arising from the GNKEs can be further tuned as shown in the insets (m) and (n) for the operating frequencies at f_{H}, and f_{I}, adding more flexibilities in manipulating the particle scattering.

To gain a deeper insight into the phenomenon, we aim to develop an analytical theory to discover the physical mechanism. The ASA is a direct evidence to witness the emergence of GNKEs and its dependence on the Mie resonance as well as the permittivity of the ENZ background medium is also apparent. Therefore, the theoretical approach starts with the calculation of ASA for the interacting multipolar modes and regarding the multipolar modes with the AMCs $m = 0$ and $m = -1$ the ASA is

$$\Gamma_{0\&-1}(\theta) = |(\xi_0 + i\zeta_0) + (\xi_{-1} + i\zeta_{-1})e^{-i\theta}|, \tag{3}$$

where ξ_0, ξ_{-1} and ζ_0, ζ_{-1} are the real and imaginary parts for the Mie coefficients S_0 and S_{-1}, respectively. By differentiating the ASA $\Gamma_{0\&-1}(\theta)$ with respect to the polar angle θ and setting $\Gamma'_{0\&-1}(\theta) = 0$, the polar angle $\theta_{\max}^{0\&-1}$ corresponding to the maximum scattering amplitude can be acquired after some mathematical manipulations:

$$\tan\theta_{\max}^{0\&-1} = \frac{\frac{\zeta_{-1}}{\xi_{-1}} - \frac{\zeta_0}{\xi_0}}{1 + \frac{\zeta_{-1}}{\xi_{-1}} \cdot \frac{\zeta_0}{\xi_0}} = \tan(\Phi_{-1} - \Phi_0), \tag{4}$$

with

$$\Phi_0 = \arctan\frac{\zeta_0}{\xi_0}, \quad \Phi_{-1} = \arctan\frac{\zeta_{-1}}{\xi_{-1}}. \tag{5}$$

As a result, the scattering direction is determined by the phase difference between the Mie coefficients S_0 and S_{-1}, namely,

$$\theta_{\max}^{0\&-1} = \Phi_{-1} - \Phi_0. \tag{6}$$

As a special case, when the Mie coefficients S_0 and S_{-1} are in phase, i.e., $\theta_{\max}^{0\&-1} = 0$, the forward scattering can be realized. This is just the case at frequency f_{F} as shown in Fig. 3, where both the amplitude and phase of S_0 and S_{-1} are the same. Accordingly,

$$\Gamma_{0\&-1}(0) = 2|S_0| = 2|S_{-1}|. \tag{7}$$

At opposite direction, namely, the backward scattering amplitude $\Gamma_{0\&-1}(\pi) = 0$. This is the reason that the first type Kerker effect is implemented.

Differently, at frequency f_{E} the GNKE is observed as shown in Fig. 3(j), where the phase difference $\Phi_{-1} - \Phi_0$ is close to $-\frac{\pi}{2}$ as can be found in Fig. 3(e). Thus the Mie coefficients satisfy $S_{-1} = S_0 e^{-i\frac{\pi}{2}}$ and the maximum value of $\Gamma_{0\&-1}(\theta)$ appears at the direction with the polar angle $\theta_{\max}^{0\&-1} = -\frac{\pi}{2}$, namely

$$\Gamma_{0\&-1}\left(-\frac{\pi}{2}\right) = 2|S_0| = 2|S_{-1}|. \tag{8}$$

At the opposite direction, the corresponding backward scattering amplitude $\Gamma_{0\&-1}(\frac{\pi}{2}) = 0$, thus explaining the realization of GNKE. Therefore, for the first kind of HMA immersed in the ENZ medium the coexistence of reciprocal and nonreciprocal Kerker effects can be observed in the vicinity of a very narrow Mie resonance, which is the unique property rarely considered by far. This implies that only a very small frequency shift can lead to the direction switching of unidirectional scattering by the first kind of HMA.

In a similar manner, we can analyze the interacting multipolar modes with the AMCs $m = 0$ and $+1$ and the corresponding ASA can be written straightforwardly as

$$\Gamma_{0\&+1}(\theta) = \left|(\xi_0 + i\zeta_0) + (\xi_{+1} + i\zeta_{+1})e^{i\theta}\right|, \tag{9}$$

where ξ_0, ξ_{+1} and ζ_0, ζ_{+1} are the real and imaginary parts for the Mie coefficients S_0 and S_{+1}, respectively. By differentiating the ASA $\Gamma_{0\&+1}(\theta)$ with respect to the polar angle θ and setting $\Gamma'_{0\&+1}(\theta) = 0$, the polar angle with the maximum scattering amplitude can be acquired after some mathematical manipulations:

$$\tan\theta_{\max}^{0\&+1} = \frac{\frac{\zeta_0}{\xi_0} - \frac{\zeta_{+1}}{\xi_{+1}}}{1 + \frac{\zeta_{+1}}{\xi_{+1}} \cdot \frac{\zeta_0}{\xi_0}} = \tan(\Phi_0 - \Phi_{+1}), \tag{10}$$

with

$$\Phi_0 = \arctan\frac{\zeta_0}{\xi_0}, \quad \Phi_{+1} = \arctan\frac{\zeta_{+1}}{\xi_{+1}}. \tag{11}$$

Therefore, the scattering direction is determined by the phase difference between the Mie coefficients S_0 and S_{+1}, namely,

$$\theta_{\max}^{0\&+1} = \Phi_0 - \Phi_{+1}. \tag{12}$$

Up to now, the Kerker effect for the case of two in-phase modes at the intersection can be analyzed in a similar manner as the case for the multipolar modes with $m = 0$ and -1 and thus the scattering direction is $\theta_{\max}^{0\&+1} = 0$. The corresponding scattering amplitude is

$$\Gamma_{0\&+1}(0) = 2|S_0| = 2|S_{+1}|. \tag{13}$$

At the opposite direction, the scattering amplitude is $\Gamma_{0\&+1}(\pi) = 0$, resulting in the formation of the first type Kerker effect. At frequency f_{G} in Fig. 3, the phase difference $\Phi_0 - \Phi_{+1}$ is close to $\frac{\pi}{2}$, resulting in the transverse upward scattering. The corresponding scattering amplitude is

$$\Gamma_{0\&+1}\left(\frac{\pi}{2}\right) = 2|S_0| = 2|S_{+1}|. \tag{14}$$

At the opposite direction, the multipolar modes are out of phase with each other so that the scattering amplitude is completely suppressed, namely, $\Gamma_{0\&+1}(-\frac{\pi}{2}) = 0$, thus giving rise to the occurrence of GNKE shown in Fig. 3(l).

For the ENZ medium with even smaller permittivity $\varepsilon_4 = 0.0025$, the nonreciprocal performance can be further tuned as visualized by the insets (m) and (n) in Fig. 3(i), where the cardioid lines of the ASAs are directed backward compared to the cases shown in the insets (j) and (l). The result shown in the inset (m) can be explained straightforwardly by examining the phase difference $\Phi_{-1} - \Phi_0$ in Fig. 3(h), which is close to $-\frac{3\pi}{4}$, corresponding to the lower backward scattering. Similarly, for the ASA shown in inset (n) the corresponding phase difference $\Phi_0 - \Phi_{+1}$ is close to $\frac{3\pi}{4}$, thus resulting in the upper backward scattering. The present theoretical approach can also be used to explain the nonreciprocal Fano resonance induced reciprocal and nonreciprocal scattering shown in Fig. 2

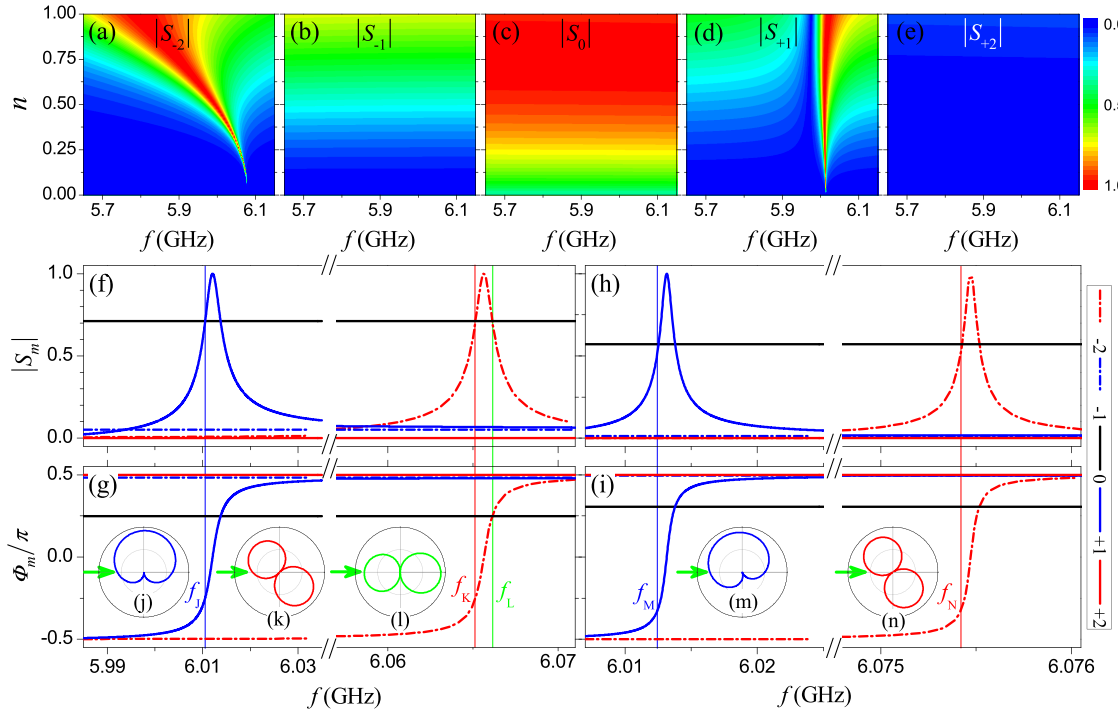

FIG. 4. Phase diagrams for the amplitudes (a) $|S_{-2}|$, (b) $|S_{-1}|$, (c) $|S_0|$, (d) $|S_{+1}|$, and (e) $|S_{+2}|$ of Mie coefficients with respect to the operating frequency f and the refractive index n of the background medium are plotted for the second kind of HMA under the BMF $H_0 = 700$ Oe. The amplitudes $|S_m|$ (f), (h) and the phase Φ_m (g), (i) of Mie coefficients are plotted as the functions of the operating frequency f for the ENZ background medium with the relative permittivity (f), (g) $\varepsilon_4 = 0.04$ (refractive index $n = 0.2$) and (h), (i) $\varepsilon_4 = 0.01$ (refractive index $n = 0.1$), respectively. Five typical operating frequencies f_J, f_K, f_L, f_M, and f_N are chosen and the corresponding ASAs are plotted in the insets (j), (k), (l), (m), and (n), respectively. The solid vertical lines mark the positions of operating frequencies and the green arrows denote the direction of incident light. All the other parameters are the same as those in Fig. 2.

by calculating the ASA arising from the Mie resonances with the AMCs $m = \pm 1$. It should be noted that the Mie resonances are very sensitive to the BMF so that the operating frequency can be flexibly shifted to the lower or higher frequency with the decrease or increase of BMF. Actually, by further minimizing the permittivity of the ENZ medium the directions of ASAs such as $\theta_{\max}^{0\&-1}$ and $\theta_{\max}^{0\&+1}$ can be turned nearly from 0 to $-\pi$ and $+\pi$, respectively, thus adding considerable degrees of freedom to manipulate the GNKEs. In addition, with the decrease of permittivity, the scattering amplitude will be weakened as well and the extreme situation corresponds to the very weak scattering, reminiscent of the invisibility of a particle.

Thus far, only the lower order modes are involved in the Kerker effect; what are the physical consequences if the higher order modes get involved? To seek out the associated scattering properties, the second kind of HMA is taken into account and the Mie coefficients as the functions of the operating frequency f and the refractive index n are plotted as shown in Figs. 4(a)–4(e). It can be found that for the Mie coefficients with the AMCs $m = 0$ and -1 the amplitudes decrease uniformly with the decrease of background refractive index n. In particular, when the refractive index n is close to zero, corresponding to the ENZ medium, the Mie coefficients for $m = -1$ and $m = +2$ are nearly zero, indicating that they are of no avail for the occurrence of Kerker effects. Differently, the linewidths of Mie resonances with the AMCs $m = +1$ and $m = -2$ become narrower and narrower, corresponding to the increase of quality factors for the Mie resonances. This implies that they will play a crucial role for the implementation of Kerker effect.

To present a precise description of the Mie resonances, both the amplitudes $|S_m|$ and the phases Φ_m of the Mie coefficients are plotted as the functions of operating frequency f for the ENZ background medium with two typical permittivities $\varepsilon_4 = 0.04$ and $\varepsilon_4 = 0.01$. The results are shown in Figs. 4(f)–4(i), where two Mie resonances are completely isolated so that the nonreciprocal Fano resonances collapse as the case for the first kind of HMA. Then, we choose five typical operating frequencies f_J, f_K, f_L, f_M, and f_N to examine the nonreciprocal scattering properties. They are positioned at the intersections between the zeroth order mode and the Mie resonances with the AMCs $m = +1$ and $m = -2$, as indicated by the solid vertical lines in Figs. 4(f) and 4(h). At frequency f_J, the GNKE is observed as visualized in Fig. 4(j) with the scattering behavior almost the same as that in Fig. 3(l), which can be interpreted in a similar manner as the situation for the first kind of HMA. The decrease of refractive index for the ENZ background medium corresponds to the change of permittivity ε_4 from 0.04 to 0.01, which gives rise to the variation of scattering direction as shown in Fig. 4(m) and the blueshift of operating frequency f_M compared to the operating frequency f_J. Regarding the higher order Mie resonance with the AMC $m = -2$, a nearly reciprocal scattering is demonstrated for the in-phase multipolar modes at the operating frequency f_L, as manifested by the nearly symmetric line shape of ASA with

respect to the incident direction. Nonetheless, for the phase difference close to $\frac{\pi}{2}$ at the operating frequency f_K the nonreciprocal scattering can be observed as displayed in Fig. 4(k). Compared to the lower order Mie resonance with $m = +1$, the relation between the phase difference and the scattering direction of ASA is different, which we have yet to explain. In addition, considering the third type Kerker effect with almost solely transverse scattering, the present nonreciprocal scattering deviated from the vertical direction can be regarded as the mutated Kerker effect, which can be considered as the GNKE as well.

To interpret this new type of GNKE associated with the higher order Mie resonance $m = -2$, the corresponding scattering direction of ASA should be derived:

$$\Gamma_{0\&-2}(\theta) = |(\xi_0 + i\zeta_0) + (\xi_{-2} + i\zeta_{-2})e^{-i2\theta}|, \tag{15}$$

where ξ_0, ξ_{-2} and ζ_0, ζ_{-2} are the real and imaginary parts for the Mie coefficients S_0 and S_{-2}, respectively. By differentiating the ASA $\Gamma_{0\&-2}(\theta)$ with respect to the polar angle θ and setting $\Gamma'_{0\&-2}(\theta) = 0$, the polar angle of the maximum amplitude can be acquired after some mathematical manipulations:

$$\tan 2\theta_{\max}^{0\&-2} = \frac{\frac{\zeta_{-2}}{\xi_{-2}} - \frac{\zeta_0}{\xi_0}}{1 + \frac{\zeta_{-2}}{\xi_{-2}} \cdot \frac{\zeta_0}{\xi_0}} = \tan(\Phi_{-2} - \Phi_0), \tag{16}$$

with

$$\Phi_0 = \arctan\frac{\zeta_0}{\xi_0}, \quad \Phi_{-2} = \arctan\frac{\zeta_{-2}}{\xi_{-2}}. \tag{17}$$

Therefore, the scattering direction $\theta_{\max}^{0\&-2}$ can be determined by the phase difference $\Phi_{-2} - \Phi_0$ according to

$$\theta_{\max}^{0\&-2} = \tfrac{1}{2}(\Phi_{-2} - \Phi_0). \tag{18}$$

Based on this theoretical approach, the reciprocal and nonreciprocal scattering properties shown in Fig. 4 can be explained. At the operating frequency f_L, the phase difference $\Phi_{-2} - \Phi_0$ is zero, resulting in

$$\Gamma_{0\&-2}(0) = 2|S_0| = 2|S_{-2}|, \tag{19}$$

$$\Gamma_{0\&-2}(\pm\pi) = 2|S_0| = 2|S_{-2}|, \tag{20}$$

$$\Gamma_{0\&-2}\left(\pm\frac{\pi}{2}\right) = 0. \tag{21}$$

The scattering amplitude in Eqs. (19)–(21) is in good agreement with the symmetric figure-of-eight profile of ASA. At the operating frequency f_K, the phase difference $\Phi_{-2} - \Phi_0$ is close to $-\frac{\pi}{2}$ and the scattering direction is thus equal to $\theta_{\max}^{0\&-2} = -\frac{\pi}{4}$, thus giving rise to

$$\Gamma_{0\&-2}\left(-\frac{\pi}{4}\right) = 2|S_0| = 2|S_{-2}|, \tag{22}$$

$$\Gamma_{0\&-2}\left(-\frac{\pi}{4} \pm \pi\right) = 2|S_0| = 2|S_{-2}|, \tag{23}$$

$$\Gamma_{0\&-2}\left(-\frac{\pi}{4} \pm \frac{\pi}{2}\right) = 0. \tag{24}$$

From the scattering amplitudes given in Eqs. (22)–(24), the GNKE shown in Fig. 4(k) can be figured out. In addition, by decreasing the permittivity of the ENZ background medium from $\varepsilon_4 = 0.04$ to $\varepsilon_4 = 0.01$ the phase difference $\Phi_{-2} - \Phi_0$ can be enlarged so that the scattering direction is deflected

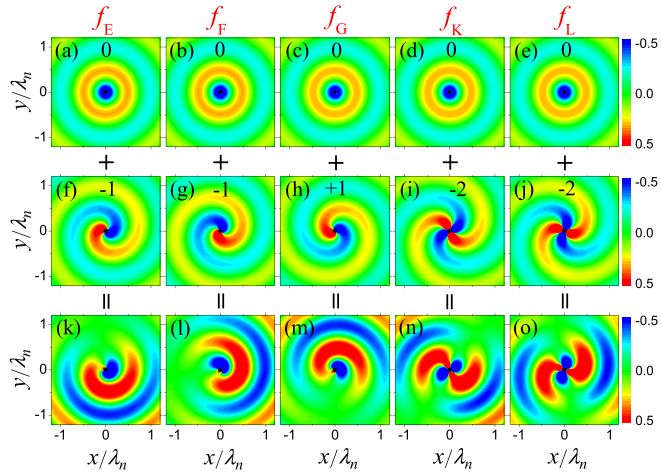

FIG. 5. Scattering field patterns for the partial waves with the AMCs (a)–(e) $m = 0$, (f),(g) $m = -1$, (h) $m = +1$, (i),(j) $m = -2$, and (k)–(o) the sum of the corresponding partial waves for the first and second kinds of HMAs immersed in the ENZ background medium with the relative permittivity $\varepsilon_4 = 0.04$ at five typical operating frequencies f_E, f_F, f_G, f_K, f_L, as marked by the vertical lines in Figs. 3 and 4. The BMF exerted on the HMAs is $H_0 = 700$ Oe, λ_n is the wavelength in the background medium with refractive index n, and the other parameters are the same as those in Fig. 2.

gradually to the vertical direction as can be observed by the inset (n) in Fig. 4. When the background permittivity ε_4 becomes infinitesimal, the phase difference approaches an extreme value close to $-\pi$. As a result, the scattering behavior nearly tends to be the transverse scattering like the third type Kerker effect. In addition, the scattering amplitude becomes very weak, similar to the case for the first kind of HMA.

The ASAs illustrate the far field scattering features, but the details of scattering fields, especially the near field scattering by the HMAs, cannot be inspected. For this reason, the electric field patterns for the scattering partial waves associated with the AMCs $m = 0, m = -1, m = +1, m = -2$ have been simulated at five typical operating frequencies f_E, f_F, f_G, f_K, f_L chosen in Figs. 3 and 4, respectively, for the first and second kinds of HMAs immersed in the ENZ background medium with the permittivity $\varepsilon_4 = 0.04$. The zeroth order modes at different operating frequencies are almost the same and exhibit central symmetry, suggesting that they do not make a contribution to the nonreciprocal performance. Differently, the Mie resonances with the AMCs $m = -1$ and $m = +1$ manifest themselves as the clockwise and counterclockwise two-fringe field patterns, respectively, which can be visualized better by plotting the maps of Poynting vectors. As a result, the complete isolation of the Mie resonance in the ENZ background medium is responsible for the generation nonreciprocal scattering. At the operating frequency f_E, the interaction between the zeroth order mode and the Mie resonance with $m = -1$ is shown in Fig. 5(k), where the destructive interference of the electric fields in the upper area can be observed and in the the lower area the electric fields interference constructively, resulting in the formation of the GNKE. Comparing panels (f) and (g), it can be found that the phase difference $\Phi_{-1}^F - \Phi_{-1}^E$ is close to $\frac{\pi}{2}$ as also quantitatively discerned in Fig. 3(e),

corresponding to the counterclockwise rotation of the field pattern. Therefore, the interference pattern is switched from the downward scattering to the forward scattering as shown in Fig. 5(l), corresponding to the first type Kerker effect. However, a weak asymmetric field profile implies the existence of a nonreciprocal feature of the near-field particle scattering, which is not discerned from the ASA in Fig. 3(k). In a similar manner, the upward scattering shown in Fig. 5(m) can be interpreted.

Differently, the scattering field patterns for the Mie resonance with $m = -2$ by the second kind of HMA is the clockwise four-fringe field pattern and its interference with the zeroth order mode results in the oblique scattering shown in Fig. 5(n), corresponding to the mutated Kerker effect shown in Fig. 4(k). As shown in Fig. 4(g), the phase difference of the Mie resonance with $m = -2$ at two operating frequencies f_{L} and f_{K} is $\frac{\pi}{2}$, which corresponds to the counterclockwise rotation of $\frac{\pi}{4}$ by examining the field patterns in Figs. 5(i) and 5(j). As a result, at frequency f_{L} the scattering field by the second kind of HMA corresponds to the counterclockwise rotation of oblique scattering in Fig. 5(n) to the horizontal scattering shown in Fig. 5(o). Similar to the case in panel (l), the asymmetric field profile with respect to the incident direction signifies an effect arising from the nonreciprocal performance, which cannot be discerned from the symmetric figure-of-eight curve of ASA in Fig. 4(l). The nonreciprocal features of the near field scattering might be significant for engineering the light-matter interactions in the oligomers composed of multiple HMAs.

Finally, it is interesting to note that due to the nonreciprocal nature of HMAs only a part of the partial waves associated with the AMCs exist, while the others are nearly suppressed as indicated in Figs. 3 and 4. For the AMC $m \neq 0$, the associated partial wave exhibits either a clockwise or counterclockwise energy vortex, signifying the emergence of orbital angular momentum (OAM). Regarding the specified operating frequencies in Fig. 5, the partial waves associated with the nonzero AMCs $m = -1$, $+1$, and -2 dominate the field patterns, giving rise to the total scattering fields characterized with the respective OAM. In addition, although the GNKEs demonstrated in the present research are just the theoretical prediction, the experimental implementation is feasible. First of all, the zero-index material can be easily designed with both the dielectric photonic crystals [86] and the magnetic metamaterials [87,88] based on the Dirac cone induced accidental degeneracy. Then, by substituting one of the unit cells in the zero-index material with the first or second kind of HMAs, the equivalent scenario of an MML subwavelength HMA immersed in the zero-index material is fulfilled. In addition, the nonreciprocal scattering in such configurations is much easier to measure in experiments compared to the cases with either nonlinear or time-varying materials involved verifications.

IV. TUNABILITY OF GNKEs BY BMFs

Due to the sensitive dependence of the magnetic medium on the BMF, the scattering properties of the subwavelength HMAs can also be controlled by tuning the BMF. To illustrate the performance, we choose three typical operating frequencies f_{E}, f_{F}, and f_{G} for the first kind of HMA immersed in the ENZ background medium with the relative permittivity $\varepsilon_4 = 0.04$. At the operating frequency f_{E}, the amplitudes and the phases of Mie coefficients S_m are plotted as the functions of the BMF as shown in Figs. 6(a) and 6(e), respectively, where two intersections can be found as marked by the solid vertical lines. The intersection on the right hand side is the same as that in Fig. 3(j), corresponding to the GNKE under the BMF $H_0 = 700$ Oe, while for the intersection on the left hand side the phase difference is zero so that the first type Kerker effect is observed as indicated by the red solid line in Fig. 6(i). Therefore, by tuning the BMF from $H_0 = 700$ Oe to 667 Oe the particle scattering can be transformed from the GNKE to the first type Kerker effect and vice versa. At the operating frequency f_{F}, the corresponding results are shown in Figs. 6(b), 6(f) and 6(j), where the scattering performance can be switchable by tuning the BMF between 700 Oe and 730 Oe with the blue solid line marking the first type Kerker effect, corresponding to that shown in panel (j). Similarly, for the Mie resonance with the AMC $m = +1$ the switchable Kerker effect is also shown to be controllable by a BMF as illustrated in Fig. 6(k), where only a smaller change of the BMF is required due to the narrowed linewidth of Mie resonance compared to the case for the AMC $m = -1$. For the second kind of subwavelength HMA, the operating frequency f_{K} is chosen to examine the tunable scattering properties and the corresponding results are shown in Figs. 6(d), 6(h) and 6(l), respectively, where the reconfigurable GNKE can be implemented with an even smaller change of the BMF but the rotation angle between two statuses is relatively smaller compared to the first kind of HMA. Besides, with decreasing the permittivity of the ENZ background medium, the linewidth of the multipolar Mie resonances can be narrowed further and the switchable GNKEs are more sensitive to the BMF, which might be useful for the detection of the ENZ medium. It should be pointed out that the tunability of the GNKEs can also be triggered by reversing the magnetization, by which the scattering performance can be switched between the mth and $-m$th order Mie resonances.

By tuning the BMF, the switchable GNKE is demonstrated in the last section, which adds considerable flexibility in the manipulation of scattering properties by the subwavelength HMAs. Actually, we can also visualize the tunability of the scattering performance by a BMF from another point of view by considering the fact that the response of diverse multipolar Mie resonances to the BMF behaves rather differently. For this purpose, the Mie resonances with both the lower order AMC $m = +1$ and the higher order AMC $m = -2$ arising from the second kind of HMA are plotted as the functions of the operating frequency f and the BMF H_0, as shown in Figs. 7(a) and 7(b), respectively. With the increase of the BMF, the operating frequencies for both Mie resonances exhibit blueshifts, as indicated by the rightward inclination of the narrow fringes. The lower order Mie resonance with the AMC $m = +1$ exhibits a more sensitive response to the BMF in that the operating frequency spans a wider frequency range. In addition, the corresponding linewidth also becomes narrower and narrower at higher frequency. The linewidth for the higher order Mie resonance with the AMC $m = -2$ is relatively narrower in the whole frequency range. To present a clear picture in regard to the frequency dependence, the Mie resonances are plotted

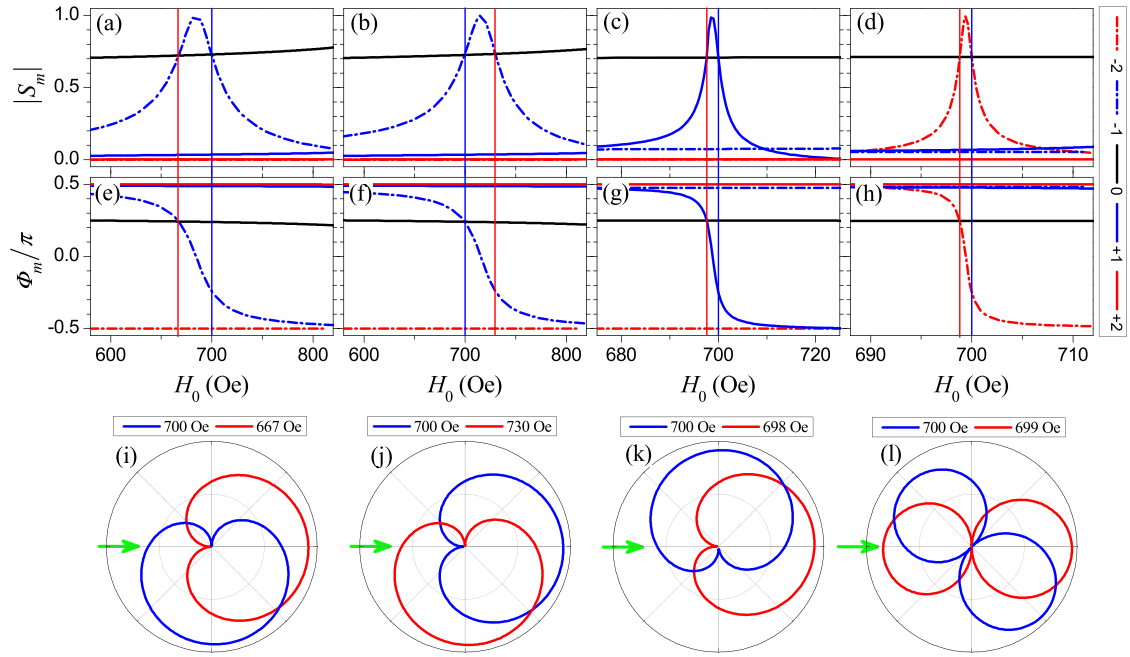

FIG. 6. Amplitudes $|S_m|$ and the phases Φ_m of Mie coefficients S_m are plotted as the functions of the BMF at the operating frequencies (a), (e) f_E, (b), (f) f_F, and (c), (g) f_G for the first kind of HMA and at the operating frequency (d), (h) f_K for the second kind of HMA immersed in the ENZ background medium with the relative permittivity $\varepsilon_4 = 0.04$ (refractive index $n = 0.2$). The switchable ASAs controlled by the BMFs at the operating frequencies (i) f_E, (j) f_F, (k) f_G, and (l) f_K, respectively. The solid vertical lines mark the corresponding two typical BMFs at four different operating frequencies and the other parameters are the same as those in Fig. 2.

as the functions of operating frequency f for the HMA under two typical BMFs $H_0 = 300$ Oe and $H_0 = 1100$ Oe, respectively, as shown in Figs. 7(c) and 7(d). Under the weaker BMF with $H_0 = 300$ Oe, two Mie resonances with the AMCs $m = +1$ and $m = -2$ are completely separated and the lower order Mie resonance appears at lower frequency as shown in Fig. 7(c). Nevertheless, under the stronger BMF $H_0 = 1100$ Oe the blueshift of the operating frequency for the lower order Mie resonance with $m = +1$ is more evident than that for the higher Mie resonance with $m = -2$ so that the lower order Mie resonance appears at the even higher frequency, thus giving rise to the frequency reversing by tuning the BMF. It

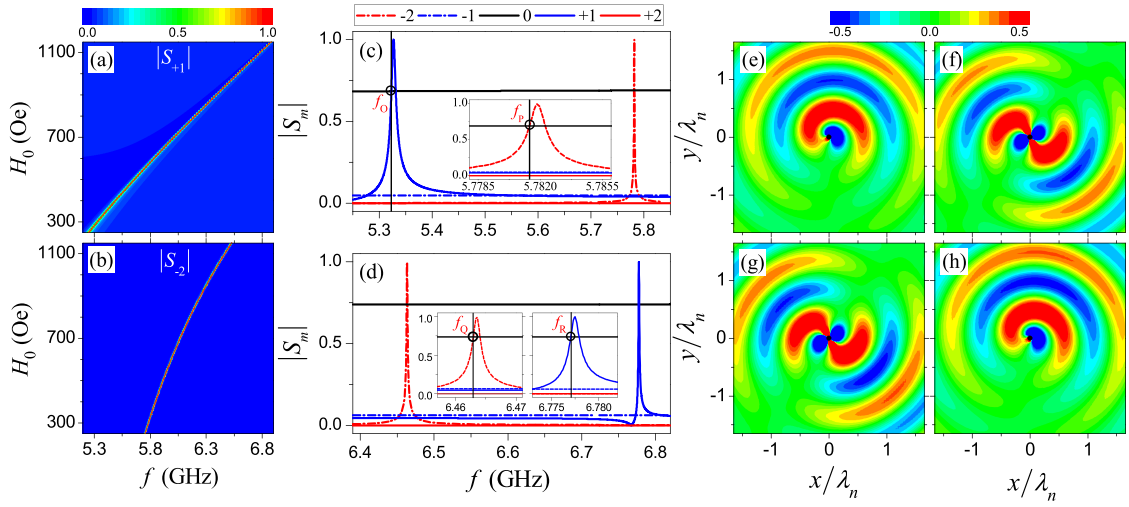

FIG. 7. Phase diagrams showing the amplitudes of Mie coefficients (a) $|S_{+1}|$ and (b) $|S_{-2}|$ as the functions of the operating frequency f and the BMF H_0 for the second kind of subwavelength HMA immersed in the ENZ background medium with the relative permittivity $\varepsilon_4 = 0.04$ (refractive index $n = 0.2$). The amplitudes of Mie coefficients $|S_m|$ are plotted as the function of the operating frequency f for the HMA under two typical BMFs (c) $H_0 = 300$ Oe and (d) $H_0 = 1100$ Oe, respectively, with the insets showing the amplified view of the Mie resonances. The scattering field patterns at four chosen operating frequencies (e) f_O, (f) f_P, (g) f_Q, and (h) f_R, respectively, to illustrate the frequency reversing of the GNKEs associated with the lower and higher order Mie resonances. The vertical lines mark the chosen operating frequencies and the other parameters are the same as those in Fig. 2.

is noted that compared to the aforementioned nonreciprocal Fano resonances the linewidth of Mie resonance becomes much narrower, resulting in the nearly single operating frequency of GNKE under a fixed BMF. This feature implies the sensitivity of operating frequency to the background medium and the BMF, giving rise to the potential applications for sensing effect.

To illustrate the physical consequence due to the frequency reversing, four typical frequencies f_O, f_P, f_Q, and f_R are chosen at the intersections between the zeroth order mode and the multipolar Mie resonances with the AMCs $m = +1$ and $m = -2$ as marked by the solid vertical lines in Figs. 7(c) and 7(d). In particular, for the narrow Mie resonances the chosen frequencies are also shown in the insets and marked by the hollow circles. The scattering field patterns have been simulated at four chosen frequencies and the results are shown in Figs. 7(e)–7(h), where the GNKE with the upward scattering is observed for the lower order Mie resonance with the AMC $m = +1$ at the operating frequency f_O. At the higher operating frequency f_R, a similar scattering field pattern is observed, indicating that for the HMA immersed in the same ENZ background medium the BMF only alters the operating frequency but the field maps of GNKEs exhibit no evident changes. By comparing the scattering field patterns in Figs. 7(f) and 7(g), it can be found that with the change of the operating frequency from f_P to f_Q the field maps are almost the same, similar to the occasion for the lower order Mie resonance. By the way, the frequency reversing indicates that the interaction between the Mie resonances can be flexibly tuned by delicately controlling the frequency difference between the Mie resonances beyond the Kerker effects considered in present research. Interestingly, the meta-atoms can also be arranged periodically to functionalize as metasurfaces so that the reconfigurable nonreciprocal lattice Kerker effects might be realized as the generalized lattice Kerker effect observed in the phase-change metasurface [89] and the parity-time symmetry metasurface [90].

V. CONCLUSIONS

In summary, within the framework of generalized Mie theory the scattering properties of the MML subwavelength HMAs can be rigorously solved. Two kinds of HMAs are theoretically designed with the first kind of HMA possessing only the lower order Mie resonances with the AMCs $m = \pm 1$, resulting in the formation of nonreciprocal Fano resonance. But for the second kind of HMA both the lower and higher order Mie resonances with the AMCs $m = \pm 1$ and -2 come into appearance; their combining interaction leads to the enhancement of nonreciprocal Fano resonance. As a result, the unidirectional scattering can be observed by examining the ASAs and the electric near-field patterns. By altering the background medium from the air to the ENZ medium, the multipolar Mie resonances are narrowed except for the zeroth order mode, which corresponds to the Mie resonances with infinitely high quality factors, resulting in the isolation of Mie resonances and thus triggering the collapse of nonreciprocal Fano resonances for both kinds of HMAs. Interestingly, the interaction between the narrowed Mie resonances and the zeroth order mode gives rise to the occurrence of either the nearly reciprocal Kerker effects or the GNKEs with cardioid and figure-of-eight ASAs, respectively, for the lower order Mie resonances with $m = \pm 1$ and the higher order Mie resonance with $m = -2$. To better interpret the phenomenon, the theoretical approach is developed, based on which the rules are established for the GNKEs associated with both the lower and higher order multipolar Mie resonances. More importantly, the scattering performance can be flexibly modulated by the BMF so that the nearly reciprocal Kerker effect and the GNKEs can be switched to each other. In addition, the different frequency dependence of Mie resonances also results in the frequency reversing. The present work concentrates on the single-particle scattering; we can expect more sophisticated phenomena by considering multiple particle scattering via engineering the mutual interactions between subwavelength HMAs and, furthermore, the subwavelength HMAs can also be used as the building blocks to construct metamaterials and metasurfaces with particular functionalities.

ACKNOWLEDGMENTS

This research was funded by the National Natural Science Foundation of China (Grant No. 11574275) and Zhejiang Provincial Natural Science Foundation of China (Grant No. LR16A040001). Q.L. was supported by the Middle-aged and Young Teachers' Basic Ability Promotion Project of Guangxi Province (Grant No. 2022KY1604).

APPENDIX: MIE THEORY ON THE MML SUBWAVELENGTH HMA

The MML subwavelength HMA considered in present research is a three-layered composite cylindrical particle with the magnetic medium sandwiched by dielectric-material layers, which is schematically shown in Fig. 1 where the related parameters are identified and the axis of HMA is along the z axis. The magnetic medium is single-crystal YIG ferrite with the magnetic permeability a second-rank tensor given by Eq. (1), which takes effect only for the electromagnetic waves of TM polarization with the electric field polarized along the z direction. The scattering properties of the HMA can be rigorously solved within the framework of Mie theory. As the first step, the electromagnetic waves in different regions should be expanded into the summation of vector cylindrical wave functions. Region I is the core part of HMA, where the medium is isotropic dielectric material with the relative permittivity ε_1 and the relative permeability μ_1. The electric and magnetic fields are

$$\boldsymbol{E}_1 = \sum_m E_m q_m^1 \boldsymbol{N}_m^{(1)}(k_1, \boldsymbol{r}), \tag{A1}$$

$$\boldsymbol{H}_1 = \frac{\omega\varepsilon_1}{ik_1} \sum_m E_m q_m^1 \boldsymbol{M}_m^{(1)}(k_1, \boldsymbol{r}), \tag{A2}$$

where the prefactor $E_m = i^m |E_0|$, with E_0 the amplitude of the electromagnetic wave, q_m^1 the expansion coefficients, and $k_1 = \frac{\omega}{c}\sqrt{\varepsilon_1}\sqrt{\mu_1}$ the wave number of the electromagnetic wave in region I. Region II is the magnetic layer with the relative

permittivity ε_2 and the permeability $\hat{\mu}$. The electric and magnetic fields are

$$\boldsymbol{E}_2 = \sum_m E_m\left[q_m^2 \boldsymbol{N}_m^{(1)}(k_2,\boldsymbol{r}) - b_m^2 \boldsymbol{N}_m^{(3)}(k_2,\boldsymbol{r})\right], \tag{A3}$$

$$\boldsymbol{H}_2 = \frac{\omega\varepsilon_2}{ik_2}\sum_m E_m\left\{q_m^2\left[\boldsymbol{M}_m^{(1)}(k_2,\boldsymbol{r}) - i\frac{\mu_\kappa}{\mu_r}\boldsymbol{L}_m^{(1)}(k_2,\boldsymbol{r})\right] - b_m^2\left[\boldsymbol{M}_m^{(3)}(k_2,\boldsymbol{r}) - i\frac{\mu_\kappa}{\mu_r}\boldsymbol{L}_m^{(3)}(k_2,\boldsymbol{r})\right]\right\}, \tag{A4}$$

where q_m^2 and b_m^2 are the expansion coefficients of inward and outward electromagnetic waves in region II, respectively, while $k_2 = \frac{\omega}{c}\sqrt{\varepsilon_2}\sqrt{\frac{\mu_r^2-\mu_\kappa^2}{\mu_r}}$ is the wave number of the electromagnetic wave in region II. Region III is the outmost layer of the HMA with the relative permittivity ε_3 and the relative permeability μ_3 and the electric and magnetic fields can be expanded in a similar manner,

$$\boldsymbol{E}_3 = \sum_m E_m\left[q_m^3 \boldsymbol{N}_m^{(1)}(k_3,\boldsymbol{r}) - b_m^3 \boldsymbol{N}_m^{(3)}(k_3,\boldsymbol{r})\right], \tag{A5}$$

$$\boldsymbol{H}_3 = \frac{\omega\varepsilon_3}{ik_3}\sum_m E_m\left[q_m^3 \boldsymbol{M}_m^{(1)}(k_3,\boldsymbol{r}) - b_m^3 \boldsymbol{M}_m^{(3)}(k_3,\boldsymbol{r})\right], \tag{A6}$$

where q_m^3 and b_m^3 are the expansion coefficients of inward and outward electromagnetic wave in region III, respectively, while $k_3 = \frac{\omega}{c}\sqrt{\varepsilon_3}\sqrt{\mu_3}$ is the wave number of the electromagnetic wave propagating within region III. Region IV is the background medium with the relative permittivity ε_4 and the relative permeability μ_4 and the electric and magnetic fields are

$$\boldsymbol{E}_4 = \sum_m E_m\left[q_m^4 \boldsymbol{N}_m^{(1)}(k_4,\boldsymbol{r}) - b_m^4 \boldsymbol{N}_m^{(3)}(k_4,\boldsymbol{r})\right], \tag{A7}$$

$$\boldsymbol{H}_4 = \frac{\omega\varepsilon_4}{ik_4}\sum_m E_m\left[q_m^4 \boldsymbol{M}_m^{(1)}(k_4,\boldsymbol{r}) - b_m^4 \boldsymbol{M}_m^{(3)}(k_4,\boldsymbol{r})\right], \tag{A8}$$

where q_m^4 and b_m^4 are the expansion coefficients of incident and scattered waves in region IV, respectively, while $k_4 = \frac{\omega}{c}\sqrt{\varepsilon_4}\sqrt{\mu_4}$ is the wave number of the electromagnetic wave propagating in region IV. The vector cylindrical wave functions $\boldsymbol{L}_m^{(J)}$, $\boldsymbol{M}_m^{(J)}$, and $\boldsymbol{N}_m^{(J)}$ used in the above formulas are defined as

$$\boldsymbol{L}_m^{(J)}(k,\boldsymbol{r}) = \left[\frac{dz_m^{(J)}(x)}{dx}\hat{\boldsymbol{e}}_r + \frac{im}{x}z_m^{(J)}(x)\hat{\boldsymbol{e}}_\phi\right]e^{im\phi}, \tag{A9}$$

$$\boldsymbol{M}_m^{(J)}(k,\boldsymbol{r}) = \left[\frac{im}{x}z_m^{(J)}(x)\hat{\boldsymbol{e}}_r - \frac{dz_m^{(J)}(x)}{dx}\hat{\boldsymbol{e}}_\phi\right]e^{im\phi}, \tag{A10}$$

$$\boldsymbol{N}_m^{(J)}(k,\boldsymbol{r}) = z_m^{(J)}(x)e^{im\phi}\hat{\boldsymbol{e}}_z, \tag{A11}$$

where $x = kr$ and $z_m^{(J)}(x)$ corresponds to either the mth order Bessel function $J_m(x)$ for the superscript $J = 1$ or the mth order Hankel function of the first kind $H_m^{(1)}(x)$ for the superscript $J = 3$.

Then, the scattering properties of HMA can be solved by matching the boundary conditions at three interfaces with $r = r_1$, $r = r_2$, and $r = r_s$,

$$\boldsymbol{E}_1 \times \hat{\boldsymbol{e}}_r|_{r=r_1} = \boldsymbol{E}_2 \times \hat{\boldsymbol{e}}_r|_{r=r_1}, \tag{A12}$$

$$\begin{aligned}\boldsymbol{H}_1 \times \hat{\boldsymbol{e}}_r|_{r=r_1} &= \boldsymbol{H}_2 \times \hat{\boldsymbol{e}}_r|_{r=r_1},\\ \boldsymbol{E}_2 \times \hat{\boldsymbol{e}}_r|_{r=r_2} &= \boldsymbol{E}_3 \times \hat{\boldsymbol{e}}_r|_{r=r_2},\\ \boldsymbol{H}_2 \times \hat{\boldsymbol{e}}_r|_{r=r_2} &= \boldsymbol{H}_3 \times \hat{\boldsymbol{e}}_r|_{r=r_2},\end{aligned} \tag{A13}$$

$$\begin{aligned}\boldsymbol{E}_3 \times \hat{\boldsymbol{e}}_r|_{r=r_s} &= \boldsymbol{E}_4 \times \hat{\boldsymbol{e}}_r|_{r=r_s},\\ \boldsymbol{H}_3 \times \hat{\boldsymbol{e}}_r|_{r=r_s} &= \boldsymbol{H}_4 \times \hat{\boldsymbol{e}}_r|_{r=r_s}.\end{aligned} \tag{A14}$$

Substituting the corresponding electric and magnetic fields into the above boundary conditions Eqs. (A12), (A13), and (A14), we can derive six linear equations. It is noted that the continuity of electromagnetic wave corresponds to the equality of each order of linear equations. Aa a result, the expansion coefficients in regions I, II, III, and IV can be obtained. Concretely,

$$\frac{q_m^1}{q_m^2} = \frac{H_m^{(1)}(k_2r_1)\mathcal{J}_m(k_2r_1) - \mathcal{H}_m(k_2r_1)J_m(k_2r_1)}{\frac{\omega\varepsilon_1}{ik_1}H_m^{(1)}(k_2r_1)J_m'(k_1r_1) - J_n(k_1r_1)\mathcal{H}_m(k_2r_1)}, \tag{A15}$$

$$\frac{q_m^2}{q_m^3} = \frac{\frac{2i}{k_3r_2}}{\mathcal{T}_m\left(\frac{b_m^2}{q_m^2}, k_2r_2\right)H_m^{(1)'}(k_3r_2) - \frac{\varepsilon_2k_3}{k_2\varepsilon_3}H_m^{(1)}(k_3r_2)\widetilde{\mathcal{T}}_m\left(\frac{b_m^2}{q_m^2}, k_2r_2\right)}, \tag{A16}$$

$$\frac{q_m^3}{q_m^4} = \frac{\frac{2i}{k_4r_s}}{H_m^{(1)'}(k_4r_s)\mathcal{T}_m\left(\frac{b_m^3}{q_m^3}, k_3r_s\right) - \frac{\varepsilon_3k_4}{\varepsilon_4k_3}\overline{\mathcal{T}}_m\left(\frac{b_m^3}{q_m^3}, k_3r_s\right)H_m^{(1)}(k_4r_s)}, \tag{A17}$$

$$\frac{b_m^2}{q_m^2} = \frac{J_m(k_2r_1)J_m'(k_1r_1) - \mathcal{J}_m(k_2r_1)J_m(k_1r_1)}{H_m^{(1)}(k_2r_1)J_m'(k_1r_1) - \mathcal{H}_m(k_2r_1)J_m(k_1r_1)}, \tag{A18}$$

$$\frac{b_m^3}{q_m^3} = \frac{\frac{k_2\varepsilon_3}{\varepsilon_2k_3}J_m'(k_3r_2)\mathcal{T}_m\left(\frac{b_m^2}{q_m^2}, k_2r_2\right) - J_m(k_3r_2)\widetilde{\mathcal{T}}_m\left(\frac{b_m^2}{q_m^2}, k_2r_2\right)}{\frac{k_2\varepsilon_3}{\varepsilon_2k_3}H_m^{(1)}(k_3r_2)\mathcal{T}_m\left(\frac{b_m^2}{q_m^2}, k_2r_2\right) - H_m^{(1)}(k_3r_2)\widetilde{\mathcal{T}}_m\left(\frac{b_m^2}{q_m^2}, k_2r_2\right)}, \tag{A19}$$

$$\frac{b_m^4}{q_m^4} = \frac{\mathcal{T}_m\left(\frac{b_m^3}{q_m^3}, k_3r_s\right)J_m'(k_4r_s) - \frac{\varepsilon_3k_4}{\varepsilon_4k_3}\overline{\mathcal{T}}_m\left(\frac{b_m^3}{q_m^3}, k_3r_s\right)J_m(k_4r_s)}{\mathcal{T}_m\left(\frac{b_m^3}{q_m^3}, k_3r_s\right)H_m^{(1)'}(k_4r_s) - \frac{\varepsilon_3k_4}{\varepsilon_4k_3}\overline{\mathcal{T}}_m\left(\frac{b_m^3}{q_m^3}, k_3r_s\right)H_m^{(1)}(k_4r_s)}, \tag{A20}$$

with

$$\mathcal{J}_m(x) = J_m'(x) - m\frac{\mu_\kappa}{x\mu_r}J_m(x), \quad \mathcal{H}_m(x) = H_m^{(1)'}(x) - m\frac{\mu_\kappa}{x\mu_r}H_m^{(1)}(x), \tag{A21}$$

$$\mathcal{T}_m(y,x) = J_m(x) - yH_m^{(1)}(x), \quad \overline{\mathcal{T}}_m(y,x) = J_m'(x) - yH_m^{(1)'}(x), \tag{A22}$$

and $\widetilde{\mathcal{T}}_m(y,x) = \mathcal{J}_m(x) - y\mathcal{H}_m(x)$. In Eq. (A20), the dimensionless quantity $\frac{b_m^4}{q_m^4}$ is the ratio of expansion coefficients for the scattered and incident partial waves on the HMA, namely, the mth order Mie coefficient. For convenience, we define

$$S_m = \frac{b_m^4}{q_m^4}. \tag{A23}$$

With the Mie coefficients at hand, the NSCS of the HMA can be evaluated according to formula [91,92]

$$Q_{\text{sca}} = \sum_{m=-\infty}^{+\infty} |S_m|^2. \tag{A24}$$

The angular scattering amplitude, which is used to measure the directivity of scattering field by the HMA, can also be acquired in terms of [29,93]

$$\Gamma(\theta) = \left| \sum_{m=-\infty}^{+\infty} S_m e^{im\theta} \right|, \tag{A25}$$

where θ is the polar angle in Cartesian coordinate. In present research, the incident plane wave is along the x axis so that the polar angle θ can also be considered as the angle between the scattering field and the incident wave.

[1] G. Bautista, M. J. Huttunen, J. Mäkitalo, J. M. Kontio, J. Simonen, and M. Kauranen, Second-harmonic generation imaging of metal nano-objects with cylindrical vector beams, Nano Lett. **12**, 3207 (2012).

[2] X. Jin, S. W. Ye, W. Q. Cheng, J. J. Hou, W. Z. Jin, T. Y. Sheng, L. P. Hou, J. H. Marsh, Y. F. Yu, M. Sun, B. Ni, X. F. Liu, and J. C. Xiong, Sub-wavelength visualization of near-field scattering mode of plasmonic nano-cavity in the far-field, Nanophotonics **12**, 297 (2023).

[3] J. C. Harris, M. A. Scully, and E. S. Day, Cancer cell membrane-coated nanoparticles for cancer management, Cancers **11**, 1836 (2019).

[4] M. Fan, Y. Han, S. T. Gao, H. Y. Yan, L. Z. Cao, Z. H. Li, X. J. Liang, and J. C. Zhang, Ultrasmall gold nanoparticles in cancer diagnosis and therapy, Theranostics **10**, 4944 (2020).

[5] C. Alcala-Jornod, H. van der Bergh, and M. J. Rossi, Can soot particles emitted by airplane exhaust contribute to the formation of aviation contrails and cirrus clouds? Geophys. Res. Lett. **29**, 1 (2002).

[6] F. Moulin, M. Devel, and S. Picaud, Optical properties of soot nanoparticles, J. Quant. Spectrosc. Radiat. Transfer **109**, 1791 (2008).

[7] Y. Li, C. Jing, L. Zhang, and Y. T. Long, Resonance scattering particles as biological nanosensors in vitro and in vivo, Chem. Soc. Rev. **41**, 632 (2012).

[8] A. B. Taylor and P. Zijlstra, Single-molecule plasmon sensing: Current status and future prospects, ACS Sensors **2**, 1103 (2017).

[9] H. Hilal, Q. Zhao, J. Kim, S. Lee, M. N. Haddadnezhad, S. Yoo, S. Lee, W. Park, W. Park, J. Lee, J. W. Lee, I. Jung, and S. Park, Three-dimensional nanoframes with dual rims as nanoprobes for biosensing, Nat. Commun. **13**, 4813 (2022).

[10] M. I. Mishchenko, L. D. Travis, and A. A. Lacis, *Scattering, Absorption, and Emission of Light by Small Particles* (Cambridge University Press, Cambridge, UK, 2002).

[11] F. Monticone and A. Alù, Metamaterial, plasmonic and nanophotonic devices, Rep. Prog. Phys. **80**, 036401 (2017).

[12] A. H. Dorrah and F. Capasso, Tunable structured light with flat optics, Science **376**, eabi6860 (2022).

[13] Z. C. Ruan and S. H. Fan, Superscattering of light from subwavelength nanostructures, Phys. Rev. Lett. **105**, 013901 (2010).

[14] C. Qian, X. Lin, Y. Yang, X. Y. Xiong, H. P. Wang, E. P. Li, I. Kaminer, B. L. Zhang, and H. S. Chen, Experimental observation of superscattering, Phys. Rev. Lett. **122**, 063901 (2019).

[15] A. Alù and N. Engheta, Multifrequency optical invisibility cloak with layered plasmonic shells, Phys. Rev. Lett. **100**, 113901 (2008).

[16] G. P. Zouros, G. D. Kolezas, E. Almpanis, and K. L. Tsakmakidis, Three-dimensional giant invisibility to superscattering enhancement induced by Zeeman-split modes, ACS Photon. **8**, 1407 (2021).

[17] B. Luk'yanchuk, N. I. Zheludev, S. A. Maier, N. J. Halas, P. Nordlander, H. Giessen, and C. T. Chong, The Fano resonance in plasmonic nanostructures and metamaterials, Nat. Mater. **9**, 707 (2010).

[18] M. F. Limonov, M. V. Rybin, A. N. Poddubny, and Y. S. Kivshar, Fano resonances in photonics, Nat. Photon. **11**, 543 (2017).

[19] P. P. Vabishchevich, S. Liu, M. B. Sinclair, G. A. Keeler, G. M. Peake, and I. Brener, Enhanced second-harmonic generation using broken symmetry III-V semiconductor Fano metasurfaces, ACS Photon. **5**, 1685 (2018).

[20] Y. C. Fan, X. He, F. L. Zhang, W. Q. Cai, C. Li, Q. H. Fu, N. V. Sydorchuk, and S. L. Prosvirnin, Fano-resonant hybrid metamaterial for enhanced nonlinear tunability and hysteresis behavior, Research **2021**, 9754083 (2021).

[21] Y. Yu, W. Q. Xue, E. Semenova, K. Yvind, and J. Mørk, Demonstration of a self-pulsing photonic crystal Fano laser, Nat. Photon. **11**, 81 (2017).

[22] Y. Yu, A. Sakanas, A. R. Zali, E. Semenova, K. Yvind, and J. Mørk, Ultra-coherent Fano laser based on a bound state in the continuum, Nat. Photon. **15**, 758 (2021).

[23] H. J. Chen, S. Y. Liu, J. Zi, and Z. F. Lin, Fano resonance-induced negative optical scattering force on plasmonic nanoparticles, ACS Nano **9**, 1926 (2015).
[24] H. J. Chen, Q. Ye, Y. W. Zhang, L. Shi, S. Y. Liu, J. Zi, and Z. F. Lin, Reconfigurable lateral optical force achieved by selectively exciting plasmonic dark modes near Fano resonance, Phys. Rev. A **96**, 023809 (2017).
[25] J. Y. Tian, Q. Li, Y. Q. Yang, and M. Qiu, Tailoring unidirectional angular radiation through multipolar interference in a single-element subwavelength all-dielectric stair-like nanoantenna, Nanoscale **8**, 4047 (2016).
[26] T. Shibanuma, T. Matsui, T. Roschuk, J. Wojcik, P. Mascher, P. Albella, and S. A. Maier, Experimental demonstration of tunable directional scattering of visible light from all-dielectric asymmetric dimers, ACS Photon. **4**, 489 (2017).
[27] N. N. Li, Y. H. Lai, S. H. Lam, H. Y. Bai, L. Shao, and J. F. Wang, Directional control of light with nanoantennas, Adv. Opt. Mater. **9**, 2001081 (2021).
[28] J. Wang, Y. J. Liu, H. Y. Dong, Z. G. Dong, and K. H. Fung, Nonreciprocal transparency in asymmetric gyrotropic trimers, Phys. Rev. Res. **4**, 013147 (2022).
[29] W. Liu, A. E. Miroshnichenko, R. F. Oulton, D. N. Neshev, O. Hess, and Y. S. Kivshar, Scattering of core-shell nanowires with the interference of electric and magnetic resonances, Opt. Lett. **38**, 2621 (2013).
[30] W. Liu and Y. S. Kivshar, Generalized Kerker effects in nanophotonics and meta-optics, Opt. Express **26**, 13085 (2018).
[31] M. Kerker, D. S. Wang, and C. L. Giles, Electromagnetic scattering by magnetic spheres, J. Opt. Soc. Am. **73**, 765 (1983).
[32] W. Liu, J. F. Zhang, B. Lei, H. T. Ma, W. K. Xie, and H. J. Hu, Ultra-directional forward scattering by individual core-shell nanoparticles, Opt. Express **22**, 16178 (2014).
[33] B. S. Luk'yanchuk, N. V. Voshchinnikov, R. Paniagua-Domínguez, and A. I. Kuznetsov, Optimum forward light scattering by spherical and spheroidal dielectric nanoparticles with high refractive index, ACS Photon. **2**, 993 (2015).
[34] R. V. Mehta, R. Patel, R. Desai, R. V. Upadhyay, and K. Parekh, Experimental evidence of zero forward scattering by magnetic spheres, Phys. Rev. Lett. **96**, 127402 (2006).
[35] J. M. Geffrin, B. García-Cámara, R. Gómez-Medina, P. Albella, L. S. Froufe-Pérez, C. Eyraud, A. Litman, R. Vaillon, F. González, M. Nieto-Vesperinas, J. J. Sáenz, and F. Moreno, Magnetic and electric coherence in forward- and back-scattered electromagnetic waves by a single dielectric subwavelength sphere, Nat. Commun. **3**, 1171 (2012).
[36] J. Olmos-Trigo, D. R. Abujetas, C. Sanz-Fernández, J. A. Sánchez-Gil, and J. J. Sáenz, Optimal backward light scattering by dipolar particles, Phys. Rev. Res. **2**, 013225 (2020).
[37] A. Bag, M. Neugebauer, P. Woźniak, G. Leuchs, and P. Banzer, Transverse Kerker scattering for angstrom localization of nanoparticles, Phys. Rev. Lett. **121**, 193902 (2018).
[38] X. Zhang and A. L. Bradley, Wide-angle invisible dielectric metasurface driven by transverse Kerker scattering, Phys. Rev. B **103**, 195419 (2021).
[39] F. F. Qin, Z. Y. Zhang, K. P. Zheng, Y. Xu, S. N. Fu, Y. C. Wang, and Y. W. Qin, Transverse Kerker effect for dipole sources, Phys. Rev. Lett. **128**, 193901 (2022).
[40] J. Olmos-Trigo, C. Sanz-Fernández, A. García-Etxarri, G. Molina-Terriza, F. S. Bergeret, and J. J. Sáenz, Enhanced spin-orbit optical mirages from dual nanospheres, Phys. Rev. A **99**, 013852 (2019).
[41] Z. Zhang, Z. Y. Che, X. Y. Liang, J. Chu, J. P. Zeng, H. Huang, F. Guan, L. Shi, X. H. Liu, and J. Zi, Realizing generalized Brewster effect by generalized Kerker effect, Phys. Rev. Appl. **16**, 054017 (2021).
[42] M. Khokhar, F. A. Inam, and R. V. Nair, Kerker condition for enhancing emission rate and directivity of single emitter coupled to dielectric metasurfaces, Adv. Opt. Mater. **10**, 2200978 (2022).
[43] Z. X. Zhou, M. J. Ye, M. W. Yu, J. H. Yang, K. L. Su, C. C. Yang, C. Y. Lin, V. E. Babicheva, I. V. Timofeev, and K. P. Chen, Germanium metasurfaces with lattice Kerker effect in near-infrared photodetectors, ACS Nano **16**, 5994 (2022).
[44] L. B. Liu, F. F. Zhang, S. Murai, and K. Tanaka, Loss control with annealing and lattice Kerker effect in silicon metasurfaces, Adv. Photon. Res. **3**, 2100235 (2022).
[45] R. Alaee, A. Safari, V. Sandoghdar, and R. W. Boyd, Kerker effect, superscattering, and scattering dark states in atomic antennas, Phys. Rev. Res. **2**, 043409 (2020).
[46] H. K. Shamkhi, K. V. Baryshnikova, A. Sayanskiy, P. Kapitanova, P. D. Terekhov, P. Belov, A. Karabchevsky, A. B. Evlyukhin, Y. Kivshar, and A. S. Shalin, Transverse scattering and generalized Kerker effects in all-dielectric Mie-resonant metaoptics, Phys. Rev. Lett. **122**, 193905 (2019).
[47] G. P. Zouros, G. D. Kolezas, E. Almpanis, K. Baskourelos, T. P. Stefański, and K. L. Tsakmakidis, Magnetic switching of Kerker scattering in spherical microresonators, Nanophotonics **9**, 4033 (2020).
[48] W. J. Chen, Y. T. Chen, and W. Liu, Multipolar conversion induced subwavelength high-Q Kerker supermodes with unidirectional radiations, Laser Photon. Rev. **13**, 1900067 (2019).
[49] X. M. Zhang, Q. Zhang, Y. J. Yuan, J. P. Liu, and X. L. Liu, Ultra-directional forward scattering by a high refractive index dielectric T-shaped nanoantenna in the visible, Phys. Lett. A **384**, 126696 (2020).
[50] Y. X. Gao, L. Xu, and X. Shen, Q-factor mediated quasi-BIC resonances coupling in asymmetric dimer lattices, Opt. Express **30**, 46680 (2022).
[51] X. M. Zhang, Q. Zhang, S. J. Zeng, Z. Z. Liu, and J. J. Xiao, Dual-band unidirectional forward scattering with all-dielectric hollow nanodisk in the visible, Opt. Lett. **43**, 1275 (2018).
[52] J. W. Lv, X. M. Zhang, X. T. Yu, H. W. Mu, Q. Liu, C. Liu, T. Sun, and P. K. Chu, Forward and backward unidirectional scattering by the core-shell nanocube dimer with balanced gain and loss, Nanomaterials **10**, 1440 (2020).
[53] Y. H. Lai, X. M. Cui, N. N. Li, L. Shao, W. Zhang, J. F. Wang, and H. Q. Lin, Asymmetric light scattering on heterodimers made of Au nanorods vertically standing on Au nanodisks, Adv. Opt. Mater. **9**, 2001595 (2021).
[54] L. Lermusiaux, V. Many, P. Barois, V. Ponsinet, S. Ravaine, E. Duguet, M. Tréguer-Delapierre, and A. Baron, Toward Huygens' sources with dodecahedral plasmonic clusters, Nano Lett. **21**, 2046 (2021).
[55] H. T. Chen, A. J. Taylor, and N. F. Yu, A review of metasurfaces: physics and applications, Rep. Prog. Phys. **79**, 076401 (2016).
[56] A. I. Kuznetsov, A. E. Miroshnichenko, M. L. Brongersma, Y. S. Kivshar, and B. Luk'yanchuk, Optically resonant dielectric nanostructures, Science **354**, aag2472 (2016).

[57] Y. Kivshar and A. Miroshnichenko, Meta-optics with Mie resonances, Opt. Photon. News **28**, 24 (2017).

[58] K. L. Tsakmakidis, L. Shen, S. A. Schulz, X. Zheng, J. Upham, X. Deng, H. Altug, A. F. Vakakis, and R. W. Boyd, Breaking Lorentz reciprocity to overcome the time-bandwidth limit in physics and engineering, Science **356**, 1260 (2017).

[59] S. Y. Liu, W. L. Lu, Z. F. Lin, and S. T. Chui, Magnetically controllable unidirectional electromagnetic waveguiding devices designed with metamaterials, Appl. Phys. Lett. **97**, 201113 (2010).

[60] S. T. Chui, S. Y. Liu, and Z. F. Lin, Reflected wave of finite circulation from magnetic photonic crystals, J. Phys.: Condens. Matter **22**, 182201 (2010).

[61] J. J. Yu, H. J. Chen, Y. B. Wu, and S. Y. Liu, Magnetically manipulable perfect unidirectional absorber based on nonreciprocal magnetic surface plasmon, Europhys. Lett. **100**, 47007 (2012).

[62] Y. Y. Chen, Y. P. Zhang, L. Z. Zhao, G. F. Wen, L. Zhang, Q. T. Ba, Q. L. Luo, J. J. Yu, and S. Y. Liu, Rectifying nonreciprocal perfect absorber based on generalized effective-medium theory for composite magnetic metamaterials, Photonics **9**, 699 (2022).

[63] Z. Wang, Y. D. Chong, J. D. Joannopoulos, and M. Soljačić, Reflection-free one-way edge modes in a gyromagnetic photonic crystal, Phys. Rev. Lett. **100**, 013905 (2008).

[64] X. Y. Ao, Z. F. Lin, and C. T. Chan, One-way edge mode in a magneto-optical honeycomb photonic crystal, Phys. Rev. B **80**, 033105 (2009).

[65] Y. Poo, R. X. Wu, Z. F. Lin, Y. Yang, and C. T. Chan, Experimental realization of self-guiding unidirectional electromagnetic edge states, Phys. Rev. Lett. **106**, 093903 (2011).

[66] S. Y. Liu, W. L. Lu, Z. F. Lin, and S. T. Chui, Molding reflection from metamaterials based on magnetic surface plasmons, Phys. Rev. B **84**, 045425 (2011).

[67] M. D. Wang, R. Y. Zhang, L. Zhang, D. Y. Wang, Q. H. Guo, Z. Q. Zhang, and C. T. Chan, Topological one-way large-area waveguide states in magnetic photonic crystals, Phys. Rev. Lett. **126**, 067401 (2021).

[68] L. Z. Zhao, G. F. Wen, L. Zhang, J. X. Tong, Y. C. You, Q. T. Ba, Q. L. Luo, and S. Y. Liu, Reconfigurable unidirectional propagation of electromagnetic waves in photonic crystal waveguides, J. Opt. Soc. Am. B **39**, 2443 (2022).

[69] H. B. Wu, Q. L. Luo, H. J. Chen, Y. Han, X. N. Yu, and S. Y. Liu, Magnetically controllable nonreciprocal Goos-Hänchen shift supported by a magnetic plasmonic gradient metasurface, Phys. Rev. A **99**, 033820 (2019).

[70] H. J. Chen, W. L. Lu, J. J. Li, J. J. Yu, Z. F. Lin, C. T. Chan, and S. Y. Liu, Manipulating unidirectional edge states via magnetic plasmonic gradient metasurfaces, Plasmonics **12**, 1079 (2017).

[71] H. B. Wu, X. Xi, X. M. Li, Y. Poo, S. Y. Liu, and R. X. Wu, Manipulating electromagnetic radiation of one-way edge states by magnetic plasmonic gradient metasurfaces, Photon. Res. **10**, 610 (2022).

[72] J. X. Fu, J. Lian, R. J. Liu, L. Gan, and Z. Y. Li, Unidirectional channel-drop filter by one-way gyromagnetic photonic crystal waveguides, Appl. Phys. Lett. **98**, 211104 (2011).

[73] G. C. Tang, Y. H. Huang, J. F. Chen, Z. Y. Li, and W. Y. Liang, Controllable one-way add-drop filter based on magneto-optical photonic crystal with ring resonator and microcavities, Opt. Express **30**, 28762 (2022).

[74] M. Zhou, L. Shi, J. Zi, and Z. F. Yu, Extraordinarily large optical cross section for localized single nanoresonator, Phys. Rev. Lett. **115**, 023903 (2015).

[75] C. Wang, C. Qian, H. Hu, L. Shen, Z. J. Wang, H. P. Wang, Z. W. Xu, B. L. Zhang, H. S. Chen, and X. Lin, Superscattering of light in refractive-index near-zero environments, Prog. Electromagn. Res. **168**, 15 (2020).

[76] A. Alù and N. Engheta, Achieving transparency with plasmonic and metamaterial coatings, Phys. Rev. E **72**, 016623 (2005).

[77] D. Ploss, A. Kriesch, C. Etrich, N. Engheta, and U. Peschel, Youngs double-slit, invisible objects and the role of noise in an optical epsilon-near-zero experiment, ACS Photon. **4**, 2566 (2017).

[78] H. C. Chu, Q. Li, B. B. Liu, J. Luo, S. L. Sun, Z. H. Hang, L. Zhou, and Y. Lai, A hybrid invisibility cloak based on integration of transparent metasurfaces and zero-index materials, Light: Sci. Appl. **7**, 50 (2018).

[79] P. P. Iyer, M. Pendharkar, C. J. Palmstrøm, and J. A. Schuller, Ultrawide thermal free-carrier tuning of dielectric antennas coupled to epsilon-near-zero substrates, Nat. Commun. **8**, 472 (2017).

[80] K. D. Wang, A. Y. Liu, H. H. Hsiao, C. Genet, and T. Ebbesen, Large optical nonlinearity of dielectric nanocavity-assisted Mie resonances strongly coupled to an epsilon-near-zero mode, Nano Lett. **22**, 702 (2022).

[81] Y. Tian, Q. Liu, Y. Ma, N. Wang, and Y. Gu, Dielectric resonances of the cylindrical micro/nano cavity within epsilon-near-zero materials, Opt. Express **31**, 37789 (2023).

[82] J. G. Wu, Z. Fan, D. Q. Xiao, J. G. Zhu, and J. Wang, Multiferroic bismuth ferrite-based materials for multifunctional applications: Ceramic bulks, thin films and nanostructures, Prog. Mater. Sci. **84**, 335 (2016).

[83] K. K. Kefeni, A. M. Msagati, and B. B. Mamba, Ferrite nanoparticles: Synthesis, characterisation and applications in electronic device, Mater. Sci. Eng. B **215**, 37 (2017).

[84] D. M. Pozar, *Microwave Engineering*, 4th ed. (John Wiley & Sons, New York, 2012), p. 451.

[85] A. A. Bogdanov, K. L. Koshelev, P. V. Kapitanova, M. V. Rybin, S. A. Gladyshev, Z. F. Sadrieva, K. B. Samusev, Y. S. Kivshar, and M. F. Limonov, Bound states in the continuum and Fano resonances in the strong mode coupling regime, Adv. Photon. **1**, 016001 (2019).

[86] X. Q. Huang, Y. Lai, Z. H. Hang, H. H. Zheng, and C. T. Chan, Dirac cones induced by accidental degeneracy in photonic crystals and zero-refractive-index materials, Nat. Mater. **10**, 582 (2011).

[87] S. Y. Liu, W. K. Chen, J. J. Du, Z. F. Lin, S. T. Chui, and C. T. Chan, Manipulating negative-refractive behavior with a magnetic field, Phys. Rev. Lett. **101**, 157407 (2008).

[88] X. N. Yu, H. J. Chen, H. X. Lin, J. L. Zhou, J. J. Yu, C. X. Qian, and S. Y. Liu, Continuously tuning effective refractive index based on thermally controllable magnetic metamaterials, Opt. Lett. **39**, 4643 (2014).

[89] L. Xiong, X. Q. Luo, H. W. Ding, Y. F. Lu, and G. Y. Li, Polarization-independent resonant lattice Kerker effect in phase-change metasurface, J. Phys. D: Appl. Phys. **55**, 395107 (2022).

[90] J. Tapar, S. Kishen, and N. K. Emani, Generalized Kerker effect in PT-symmetric nanoantenna array, J. Opt. **24**, 034003 (2022).

[91] W. Liu, Superscattering pattern shaping for radially anisotropic nanowires, Phys. Rev. A **96**, 023854 (2017).

[92] R. Kumar and K. Kajikawa, Superscattering from cylindrical hyperbolic metamaterials in the visible region, Opt. Express **28**, 1507 (2020).

[93] H. W. Wu, Y. Fang, J. Q. Quan, Y. Z. Han, Y. Q. Yin, Y. Li, and Z. Q. Sheng, Multifrequency superscattering with high Q factors from a deep-subwavelength spoof plasmonic structure, Phys. Rev. B **100**, 235443 (2019).